



Published in final edited form as:

*Mol Cell*. 2019 August 08; 75(3): 644–660.e5. doi:10.1016/j.molcel.2019.07.028.

## Landscape of intercellular crosstalk in healthy and NASH liver revealed by single-cell secretome gene analysis

Xuelian Xiong<sup>1,2,3,#</sup>, Henry Kuang<sup>2,3,#</sup>, Sahar Ansari<sup>4,#</sup>, Tongyu Liu<sup>2,3,#</sup>, Jianke Gong<sup>2,5,6</sup>, Shuai Wang<sup>7</sup>, Xu-Yun Zhao<sup>2,3</sup>, Yewei Ji<sup>5</sup>, Chuan Li<sup>8</sup>, Liang Guo<sup>2,3</sup>, Linkang Zhou<sup>2,3</sup>, Zhimin Chen<sup>2,3</sup>, Paola Leon-Mimila<sup>9</sup>, Meng Ting Chung<sup>10</sup>, Katsuo Kurabayashi<sup>10</sup>, Judy Opp<sup>11</sup>, Francisco Campos-Pérez<sup>12</sup>, Hugo Villamil-Ramírez<sup>13</sup>, Samuel Canizales-Quinteros<sup>13</sup>, Robert Lyons<sup>11</sup>, Carey N. Lumeng<sup>14</sup>, Beiyang Zhou<sup>8</sup>, Ling Qi<sup>5</sup>, Adriana Huertas-Vazquez<sup>9</sup>, Aldons J. Lusic<sup>9</sup>, X.Z. Shawn Xu<sup>2,5</sup>, Siming Li<sup>2,3</sup>, Yonghao Yu<sup>7</sup>, Jun Z. Li<sup>4</sup>, Jiandie D. Lin<sup>2,3,\*</sup>

<sup>1</sup>Ministry of Education Key Laboratory of Metabolism and Molecular Medicine, Department of Endocrinology and Metabolism, Zhongshan Hospital, Fudan University, Shanghai, China

<sup>2</sup>Life Sciences Institute, University of Michigan, Ann Arbor, MI 48109

<sup>3</sup>Department of Cell & Developmental Biology, University of Michigan Medical Center, Ann Arbor, MI 48109

<sup>4</sup>Department of Human Genetics, University of Michigan Medical Center, Ann Arbor, MI 48109

<sup>5</sup>Department of Molecular and Integrative Physiology, University of Michigan Medical Center, Ann Arbor, MI 48109

<sup>6</sup>International Research Center for Sensory Biology and Technology of MOST, Key Laboratory of Molecular Biophysics of MOE, and College of Life Science and Technology, and Huazhong University of Science and Technology, Wuhan, Hubei, China

<sup>7</sup>Department of Biochemistry, University of Texas Southwestern Medical Center, Dallas, TX 75390

<sup>8</sup>Department of Immunology, School of Medicine, University of Connecticut, Farmington, CT 06030

<sup>9</sup>Department of Medicine, Division of Cardiology, David Geffen School of Medicine, Los Angeles, CA.

<sup>10</sup>Department of Mechanical Engineering, University of Michigan, Ann Arbor, MI 48105

\* Corresponding Author and Lead Contact: Jiandie Lin, Ph.D., 5437 Life Sciences Institute, University of Michigan, 210 Washtenaw Avenue, Ann Arbor, MI 48109, jdlin@umich.edu, Office: (734) 615-3512, Fax: (734) 615-0495.

# Equal contribution

Author contributions

J.D.L., X.X., H.K. and J.L. conceived the project and designed research. X.X., H.K., X.Z., Y.J., J.G., Z.C., X.Z.X., L.G., S.L., L.Q., M.C. and K.K. performed the experiments and analyzed the data. J.O. and R.L. performed scRNA-seq using the 10X Genomics platform. T.L., S.A. and J.D.L. performed sequencing data analyses. C.L. and B.Z. performed macrophage polarization analysis. F.C.P. and H.V.R. performed human sample collection and characterization. S.C.Q. performed genetic and biochemical characterization. A.J.L. and A.H.V. performed RNA-seq in human liver samples. P.L.M. performed statistical analyses of the human cohort.

Supplementary Information

One Supplementary Figure file (Figure S1–S7), seven Supplementary Tables (Supplementary Table S1–S7) and one key resource table are available online.

Competing interests

The authors declare no competing interests.

<sup>11</sup>University of Michigan DNA Sequencing Core, University of Michigan, Ann Arbor, MI 48109

<sup>12</sup>Clínica Integral de Cirugía para la Obesidad y Enfermedades Metabólicas, Hospital General Dr. Rubén Lénero, Mexico City, Mexico.

<sup>13</sup>Facultad de Química, UNAM/Instituto Nacional de Medicina Genómica (INMEGEN), Unidad de Genómica de Poblaciones Aplicada a la Salud, Mexico City, Mexico

<sup>14</sup>Department of Pediatrics and Communicable Diseases, University of Michigan Medical Center, Ann Arbor, MI 48109

## Summary

Cell-cell communication via ligand-receptor signaling is a fundamental feature of complex organs. Despite this, the global landscape of intercellular signaling in mammalian liver has not been elucidated. Here we perform single-cell RNA sequencing on non-parenchymal cells isolated from healthy and NASH mouse livers. Secretome gene analysis revealed a highly connected network of intrahepatic signaling and disruption of vascular signaling in NASH. We uncovered the emergence of NASH-associated macrophages (NAM), which are marked by high expression of Triggering Receptor Expressed on Myeloid Cells 2 (*Trem2*), as a feature of mouse and human NASH that is linked to disease severity and highly responsive to pharmacological and dietary interventions. Finally, hepatic stellate cells (HSC) serve as a hub of intrahepatic signaling via HSC-derived stellakines and their responsiveness to vasoactive hormones. These results provide unprecedented insights into the landscape of intercellular crosstalk and reprogramming of liver cells in health and disease.

## Keywords

Liver; NAFLD; NASH; single-cell; scRNA-seq; NPC; secretome; Kupffer; macrophage; Trem2; stellakine; HSC

## Introduction

The liver is the largest organ in the body that serves vital functions in nutrient and energy metabolism. Hepatocytes account for approximately 60% of the total cell population in human liver with non-parenchymal cells (NPC) constituting the rest, including liver sinusoidal endothelial cells (LSEC), the resident macrophage Kupffer cells (KC), hepatic stellate cells (HSC), cholangiocytes and diverse immune cell types (Friedman, 2008; Krenkel and Tacke, 2017; Poisson et al., 2017; Robinson et al., 2016; Tabibian et al., 2013). Dysregulations of hepatic metabolism contribute to the pathogenesis of type 2 diabetes, dyslipidemia and nonalcoholic fatty liver disease (NAFLD). NAFLD is characterized by excess fat accumulation in the liver and is strongly associated with obesity and metabolic syndrome. It has been estimated that approximately 25-30% of the adult population in the U.S. develops NAFLD, which may progress into nonalcoholic steatohepatitis (NASH), a more severe form of NAFLD that is characterized by chronic liver injury, fibrosis and inflammation (Cohen et al., 2011; Diehl and Day, 2017; Samuel and Shulman, 2018). NASH is emerging as a major cause of end-stage liver diseases, such as cirrhosis and hepatocellular

carcinoma, and as a leading indication for liver transplantation (Diehl and Day, 2017; Pais et al., 2016).

Numerous ligand-receptor signaling modalities have been delineated among the cells in the liver that illustrate a critical role of intrahepatic crosstalk in tissue homeostasis and injury response (Friedman, 2008; Krenkel and Tacke, 2017). In addition, hepatokines are emerging as important regulators of nutrient metabolism and energy balance by acting on the central nervous system and other peripheral tissues (Meex and Watt, 2017; Wang et al., 2019). Despite these, the repertoire of secreted ligands and membrane receptors and the global landscape of intercellular signaling among liver cells have not been mapped at the single-cell resolution. Further, the emergent nature of liver cell heterogeneity and reprogramming of intrahepatic paracrine crosstalk during NASH pathogenesis remain poorly understood.

Single-cell RNA sequencing (scRNA-seq) has emerged as a powerful tool to deconstruct the transcriptomes of complex tissues at the single-cell level (Gawad et al., 2016; Tanay and Regev, 2017). The advent of high-throughput single-cell profiling technologies provides a foundation for the Human Cell Atlas Project, an ambitious effort to define the molecular states of all human cell types in the body (Regev et al., 2017). Recent single-cell transcriptomic analysis of mouse tissues has revealed unprecedented molecular details on cellular heterogeneity (Han et al., 2018; Tabula Muris et al., 2018). In the liver, hepatocytes assume remarkably heterogeneous transcriptomic signatures that underlie zonation of diverse liver metabolic functions (Halpern et al., 2017). In this study, we performed single-cell RNA-seq and secretome analysis to dissect intercellular crosstalk in healthy and diet-induced NASH mouse livers. Our analyses revealed the landscape of intercellular crosstalk in mammalian liver and illustrated the complexity and richness of cell-cell signaling in liver physiology and disease. In addition, we uncovered the emergence of NASH-associated macrophages as a hallmark of mouse and human NASH that is strongly linked to disease progression and highly responsive to therapeutic interventions.

## Results

### RNA-seq and quantitative proteomic analyses of healthy and NASH mouse livers

Previous studies have established a diet-induced mouse NASH model (Amylin diet, AMLN diet) that faithfully recapitulates key features of human NASH (Clapper et al., 2013; Guo et al., 2017; Xiong et al., 2019). To explore the pathogenic mechanisms underlying NASH progression, we performed RNA-sequencing (RNA-seq) analysis on the livers from mice fed standard chow or AMLN diet for 20 weeks. We detected 311 and 461 genes that exhibited more than 2-fold decrease or increase in mRNA expression, respectively (Figure 1A and Table S1). Many of these NASH-induced genes were also elevated in the livers from a cohort of human NASH patients, compared to non-NASH individuals (Figure 1B). In parallel, we performed quantitative proteomic analysis and compared mRNA and protein expression in chow and AMLN diet-induced NASH livers. We observed remarkable concordance between RNA-seq and proteomic data (Figure 1C and S1A). As such, most of the NASH-induced genes revealed by RNA-seq exhibited increased protein expression, whereas downregulated genes were associated with reduced protein expression. Gene ontology analysis on these two differentially regulated gene sets revealed that the expression

of genes involved in lipid metabolism and oxidative reactions was suppressed following diet-induced NASH in mice (Figure 1A). In contrast, NASH-induced genes were highly enriched for the pathways responsible for extracellular matrix (ECM) remodeling (Col1a1, Mmp12), cell adhesion, phagocytosis, and immune response (Ccr2, H2-ab1, Lcn2), core biological functions of liver NPC. These observations underscore a potentially important role of liver NPC in driving NASH pathogenesis.

### Single-cell RNA sequencing analysis of liver NPC

To elucidate liver cell heterogeneity and their dynamic changes during NASH pathogenesis, we performed single-cell RNA sequencing (scRNA-seq) on liver NPC isolated from mice fed chow or AMLN diet. We obtained a total of 33,168 single-cell transcriptomes (17,788 chow; 15,380 NASH) from three pairs of mice. Compared to a recent hepatocyte scRNA-seq study illustrating metabolic zonation in the liver (Halpern et al., 2017), the coverage of the NPC population was vastly expanded in our dataset. T-distributed Stochastic Neighbor Embedding (t-SNE) visualization of the combined chow and NASH data revealed ten major clusters, which correspond to endothelial cells, macrophages, T cells, B cells, cholangiocytes, plasma B cells, dendritic cells (DC), HSC, hepatocytes, and a cluster representing dividing cells, based on marker gene expression (Figure 1D–F and Table S2). We examined the extent to which liver cell transcriptomes are conserved among species by integrating our dataset with a recent scRNA-seq study of human livers (MacParland et al., 2018). Correlation analysis indicated that major liver cell types displayed highly conserved transcriptomic signature and shared common sets of marker genes in mice and humans (Figure 1G and S1B).

All ten clusters contained cells derived from both chow and NASH mouse livers (Figure 1H and S1C–D). We observed that NASH livers accounted for over 77% of the cells in the macrophage cluster whereas chow endothelial cells disproportionately contributed to the endothelial cluster. The construction of single-cell transcriptome maps for different liver cell types allows us to assign likely cellular sources for the genes differentially expressed in NASH (Figure 1A). Remarkably, genes most specific to macrophage and HSC clusters were primarily NASH-induced genes in the liver (Figure 1I). In contrast, most of the hepatocyte-enriched genes were downregulated in NASH livers. These observations strongly suggest that NASH pathogenesis is linked to cell type-specific reprogramming of the liver cell transcriptomes.

### Single-cell analysis of secretome and receptor gene expression in the liver

Intercellular crosstalk via ligand and receptor signaling has been recognized to be a fundamental aspect of organ biology. Despite this, the repertoire of secreted ligands and membrane receptors and the global landscape of intercellular signaling among liver cells have not been mapped at the single-cell resolution. We next analyzed secretome gene expression in the liver cells to identify the cellular origins of ligands and receptors. We manually curated the mouse secretome gene list compiled from several available datasets (Wang et al., 2014). This list contained 1,272 and 755 genes that are predicted to encode secreted proteins and membrane receptors, respectively (Table S3). Among these, 305 secreted factors and 147 receptors had readily detectable mRNA expression (normalized

UMI>1.0) in our scRNA-seq dataset (Table S4). Clustering analysis of the liver secretome genes revealed remarkably cell type-specific patterns of receptor and ligand gene expression (Figure 2A). For example, *Kdr* and *Tek*, which encode receptor tyrosine kinases important for vascular development and maintenance, were enriched in the endothelial cluster, whereas *Csf1r* is abundantly expressed in the macrophage cluster. *Ccl5* and *Spp1* marked the T cell and cholangiocyte clusters, respectively. *Col1a1* and *Dcn* were abundantly expressed in HSC while *Cd79b* marked the B cell cluster (Figure 2b). Comparative analysis of secretome gene expression in mouse and human single-cell datasets revealed a highly conserved pattern of distribution among different liver cell types across species (Figure 2C and S2A). These results demonstrate that, compared to whole liver transcriptome analysis, scRNA-seq provides unparalleled sensitivity and accuracy in mapping ligand and receptor gene expression to specific cell types in the liver.

The notably restricted patterns of ligand and receptor expression illustrate potentially highly specific paracrine and autocrine connectivity in the mammalian liver. We next integrated our scRNA-seq data with a ligand-receptor interaction database (Ramilowski et al., 2015) to construct an intercellular signaling map among the liver cells. We identified the HSC, endothelial and macrophage clusters as prominent hubs for paracrine and autocrine signaling (Figure 2D and S2B). A subset of ligands and receptors remained orphan and lacked their cognate partners in this network, reflecting their potential role in inter-tissue endocrine crosstalk. We next analyzed how NASH alters secretome gene expression in the liver. Not surprisingly, mRNA and protein expression for the secretome gene set were highly correlated (Figure 2E). Remarkably, many genes encoding HSC and macrophage-enriched secreted factors and membrane receptors exhibited increased expression at both mRNA and protein levels, whereas hepatocyte-enriched genes lacked this pattern of regulation. Together, this secretome gene analysis revealed a global landscape of ligand and receptor gene expression, connectivity and alterations in NASH at single-cell resolution.

### Vascular signaling and its dysregulation during NASH pathogenesis

Endothelial cells represent the largest cluster within the NPC population, containing a total of 10,447 cells. At higher t-SNE resolution, this cluster can be further divided into four subclusters, representing periportal (Endo-pp) and pericentral (Endo-pc) endothelial cells and two clusters of liver sinusoidal endothelial cells (LSEC-1 and LSEC-2) that line the surface of liver sinusoids (Figure 3A). Clustering analysis of these four endothelial subtypes revealed unique transcriptomic signatures (Figure 3B–C and Table S5). Based on single molecule fluorescence *in situ* hybridization results reported in a recent study on liver endothelial zonation (Halpern et al., 2018), we identified a set of genes exhibiting Endo-pc enriched expression including *Wnt9b*, *Rspo3*, *Cdh13* and *Wnt2*. Endo-pp expressed high levels of *Ednrb*, *Jag1*, *Lrg1*, *Efnb1*, *Ltbp4* and *Adgrg6*, whereas LSEC-1 and LSEC-2 were marked by abundant expression of *Fcgr2b* and *Gpr182*, known LSEC markers (Poisson et al., 2017). While the LSEC transcriptomes appeared similar overall, a subset of genes exhibited enriched expression in a cluster-specific manner. These results support the notion of liver endothelial zonation and functional specialization in a manner resembling zonation of hepatocytes in the liver (Halpern et al., 2017).

To explore how NASH alters liver endothelial function, we analyzed chow and NASH endothelial transcriptomes in the scRNA-seq dataset and performed RNA-seq on LSEC isolated from chow and AMLN diet-fed mouse livers. The scRNA-seq and total RNA-seq datasets obtained for endothelial cells were remarkably consistent (Figure 3D). Compared to control, endothelial cells derived from NASH livers exhibited increased expression of genes involved in lipid metabolism, antigen presentation and chemokine release. In contrast, significant downregulation of genes involved in vascular development and homeostasis was observed in NASH liver. These NASH-induced alterations of gene expression appeared to occur in all four endothelial subclusters (Figure S3A–B). We further confirmed these findings using flow cytometry and observed that endothelial cell expression of Cxcl9 and BODIPY staining, a marker for cellular lipid accumulation, were strongly increased in LSEC isolated from NASH mouse livers (Figure 3E). This reprogramming of the endothelial transcriptome was linked to a profound disruption of the sinusoidal capillaries in the liver during diet-induced NASH (Figure 3F). Immunofluorescence staining of LSEC using polyclonal FCGR2B antibodies indicated that NASH mice had apparently lower abundance and altered histological integrity of the liver sinusoids.

As shown above, endothelial cells express a large number of membrane receptors and adhesion proteins and also secrete a number of angiocrine factors. Analysis of the endothelial secretome revealed that this cluster exhibited abundant expression of many membrane receptors for ligands important for vascular development and homeostasis, including Notch1, VEGF receptors (Kdr, Flt1, Flt4, Nrp1, Nrp2), TGF $\beta$  receptors (Tgfr2, Tgfr3, Bmpr2, Eng), Ephrin B receptor (Ephb4), and receptor tyrosine kinase (Tek, Tie1) and phosphatase (Ptpn) signaling pathways (Figure 3G). To delineate the paracrine and/or autocrine signaling network that acts on liver endothelial cells, we analyzed scRNA-seq data to identify the cellular sources of the putative ligands for these receptors. Remarkably, several ligands within this paracrine network were found to originate from the HSC, endothelial and cholangiocyte clusters. Dll4, a ligand for Notch1, Bmp2 and Efnb2 were highly expressed by endothelial cells and therefore considered angiocrine factors (Rafii et al., 2016), whereas Gdf2, Gdf10 and Bmp5 secretion appears to be restricted to HSC. Vegfa expression was most abundantly expressed by cholangiocytes. Comparative analysis of mouse and human scRNA-seq datasets revealed that the cellular sources of these ligands were highly conserved in these two species (Figure S3C).

The endothelial cluster exhibited abundant expression of several GPCRs (Calcr1, Ramp2, Gpr182), adhesion GPCRs (Adgrf5, Adgrl4), and cytokine receptors (Il6st, Lifr) (Figure 3G). Calcr1 and Ramp2 form a receptor complex for adrenomedullin, a peptide hormone that exerts pleiotropic effects on endothelial cells (Geven et al., 2018), suggesting that hepatic vascular system may be highly responsive to vasoactive endocrine hormones. Notably, mRNA expression of endothelial receptors and angiocrine factors, ligands secreted by endothelial cells, was significantly downregulated during diet-induced NASH (Figure 3H). To determine whether the disruptions of liver vascular function also occur during human NASH pathogenesis, we analyzed a published microarray dataset containing samples from 24 healthy, 20 NAFLD, and 19 NASH patients (GSE89632) (Arendt et al., 2015). Similar to mouse NASH, transcript abundance for *CXCL9* and *FABP4* was significantly increased in human NASH livers (Figure 3I). Compared to healthy control, the expression of *BMP2*,



*NRP1* and *VEGFA* was downregulated in the livers from NAFLD and NASH patients. These results illustrate profound disruptions of vascular and angiocrine signaling during NASH pathogenesis that is conserved in mice and humans.

### Emergence of NASH-associated macrophage and its molecular signature

A prominent feature of the macrophage cluster is its marked expansion during diet-induced NASH (Figure 4A). This cluster can be further divided into two groups of cells representing Kupffer cells and monocyte-derived macrophages (MDM) based on their marker gene expression profile (Figure 4B). KCs were characterized by high expression of *Adgre1* (encoding F4/80) and *Clec4f*, whereas MDM exhibited high expression of *Itgam* (*Cd11b*) and *Ccr2*, a chemokine receptor important for infiltration of circulating monocytes (Krenkel and Tacke, 2017). In contrast, *Csf1r* expression was observed in both KC and MDM subclusters. We compared our scRNA-seq data with a public microarray dataset on sorted KCs and MDMs (GSE98782) (Krenkel et al., 2018). We observed a remarkable concordance of gene expression profile using these two methods (Figure S4A), illustrating high accuracy of transcriptomic analysis based on scRNA-seq data. Clustering analysis indicated that both KC and MDM transcriptomes were altered following diet-induced NASH (Figure S4B). To determine how NASH alters the functional properties of liver macrophage populations, we developed a method to quantitatively evaluate macrophage polarization based on their gene expression signatures at the single cell level (Li et al., 2019). Here, a higher macrophage polarization index (MPI) reflects a more proinflammatory phenotype. This analysis indicated that KCs and MDMs from NASH livers exhibited a notable shift towards a proinflammatory phenotype (Figure 4C), consistent with induction of a proinflammatory environment during NASH pathogenesis.

We next analyzed macrophage heterogeneity and observed two KC populations marked by low and high *Trem2* mRNA expression (*Trem2<sup>lo</sup>* and *Trem2<sup>hi</sup>*, respectively). *Trem2* is a scavenger receptor required for phagocytosis and clearance of apoptotic cells and has been implicated in several disease conditions, including Alzheimer's disease and liver injury (Deczkowska et al., 2018; Perugorria et al., 2018). Remarkably, while both chow and NASH livers harbored *Trem2<sup>lo</sup>* KC, over 93% of *Trem2<sup>hi</sup>* KC were derived from NASH livers, indicating that this is a unique population of macrophages associated with NASH pathogenesis (Figure 4D). As such, we termed this *Trem2<sup>hi</sup>* KC population "NASH-associated macrophages" (NAM). In addition to *Trem2*, NAM also exhibited abundant expression of *Gpnmb* and *Cd9*, all of which were induced during NASH (Figure 4E). Importantly, hepatic *Trem2* and *Gpnmb* mRNA expression was strongly associated with liver injury and fibrosis in a cohort of mice with varying NASH severity (Xiong et al., 2019) (Figure 4F and S4C). To confirm the emergence of NAM during NASH pathogenesis, we performed flow cytometry using GPNMB and CD9 antibodies to detect this macrophage population (Figure 4G). Consistent with single-cell analysis, we observed a marked expansion of KC in NASH livers. While GPNMB<sup>+</sup> CD9<sup>+</sup> double positive KC were rarely detected in chow livers, they represented over 60% of KC obtained from NASH livers.

To further investigate the dynamic changes of liver macrophages during NASH pathogenesis, we performed studies in mice fed chow or CDAHFD, a choline-deficient, L-

amino acid defined HFD that contains 0.1% methionine. This diet was recently shown to induce robust NASH pathologies in mice within six weeks (Matsumoto et al., 2013). As expected, CDAHFD feeding markedly elevated plasma ALT and AST levels, induced fibrotic and inflammatory gene expression and expanded macrophage population in the liver (Figure S5A–C). In addition, hepatic Trem2 and Gpnmb mRNA expression was drastically increased in the livers from mice fed CDAHFD. Flow cytometry analysis indicated that while GPNMB<sup>+</sup> NAM were essentially absent in chow livers, this population represented over 70% of KC in the liver following CDAHFD-induced NASH (Figure 4H). GPNMB is a transmembrane protein and has been shown to undergo cleavage to release the extracellular domain into circulation (van der Lienden et al., 2018). We performed ELISA to measure the concentrations of GPNMB in plasma from healthy and NASH mice. Plasma GPNMB levels were significantly elevated in both AMLN diet and CDAHFD-induced NASH (Figure 4I), suggesting that it may provide a potential biomarker for NASH.

The emergence of NASH-specific macrophages in the liver suggests that NAM may play an important role in the pathogenesis of disease. To examine the molecular properties of NAM, we binned chow and NASH KC (25 cells per bin) into respective Trem2-negative, Trem2-low, and Trem2-high subgroups (Figure 5A). We identified a cluster of genes exhibiting a high degree of correlation with Trem2 expression. Gene ontology analysis indicated that Trem2-high macrophages had enriched expression for genes involved in endocytosis, lysosomal degradation, MHC class II antigen presentation and extracellular matrix remodeling. Macrophages express a large number of scavenger receptors including Trem2, which are responsible for the clearance of apoptotic cells and extracellular matrix during tissue injury. These results illustrate that liver resident macrophages undergo both marked expansion and functional reprogramming during NASH pathogenesis.

### Dynamic regulation of NAM in human NASH and during NASH resolution

We next explored whether human NASH is associated with induction of NAM. Analysis of a microarray dataset indicated that *TREM2* mRNA expression was increased in the livers from patients with hepatic steatosis and NASH (Figure 5B). We further examined the association between hepatic *TREM2* gene expression and NASH parameters in an independent cohort of 144 NASH patients (Hui et al., 2018; Vega-Badillo et al., 2016). We observed a remarkable association between *TREM2* expression and plasma markers of liver injury (Figure 5C). In addition, hepatic *TREM2* expression was strongly associated with the severity of steatosis, inflammation, hepatocyte ballooning, liver fibrosis and NAFLD activity score (NAS) (Figure 5D). Hepatic *GPNMB* mRNA expression was also associated with these NASH pathologies (Figure S4D). These results indicate that the induction of NAM gene signature is a common feature of mouse and human NASH pathogenesis. Further, we have demonstrated the potential for using NAM markers as a diagnostic biomarker for NASH.

Key aspects of NASH pathologies are largely reversible in response to pharmacological and/or dietary interventions (Romero-Gomez et al., 2017). We next examined whether NASH reversal is linked to reduction of Trem2<sup>hi</sup> KC and attenuation of NAM gene signature in the liver. In the first set of studies, we treated mice fed CDAHFD with Elafibranor, a dual agonist for PPAR $\alpha$  and PPAR $\delta$  that has been shown to be effective in reversing NASH



pathologies in mice (Staels et al., 2013). Compared to vehicle, Elafibranor treatment potently lowered plasma AST and ALT levels and markedly reduced the abundance of NAM in the liver, as revealed by GPNMB flow cytometry (Figure 5E–F). Hepatic gene expression analysis indicated that Elafibranor stimulated mRNA expression of genes involved in fatty acid  $\beta$ -oxidation (*Acadm*, *Acox1*) while attenuating expression of *Trem2*, *Gpnmb*, *Tnf* and *Coll1a1* (Figure 5G). Consistently, hepatic GPNMB protein expression and plasma GPNMB levels were also reduced following Elafibranor treatments in mice fed CDAHFD (Figure 5H–I). We previously demonstrated that dietary switch from AMLN diet to chow for eight weeks resulted in marked improvements of NASH pathologies in mice (Xiong et al., 2019). In this model, we also observed significantly reduced expression of *Trem2*, *Gpnmb* and *Cd9* following dietary switch (Figure 5J). Compared to AMLN group, plasma GPNMB concentrations were also lower following the AMLN to chow dietary switch (Figure 5K). These results demonstrate that NAM and their associated gene signature are highly responsive to pharmacological and dietary interventions that reverse NASH pathologies.

### The hepatic stellate cell ligand-receptor signaling network

We obtained single-cell transcriptome data for a total of 272 cells in the HSC cluster. The HSC secretome was prominent in its diversity, containing 27 and 99 genes encoding membrane proteins and secreted factors, respectively (Table S6). As expected, a large number of proteins secreted by HSC correspond to the structural proteins of ECM including collagens and proteoglycans and those involved in ECM remodeling (Figure 6A). Analysis of liver RNA-seq data indicated that, compared to healthy control, expression of many of these genes was strongly increased in NASH livers, reflecting activation of the fibrosis gene program. We next constructed a ligand-receptor signaling network on the secretome genes exhibiting enriched expression in HSC, a unique set of secreted factors that we termed “stellakines” for their stellate cell origin. This analysis revealed that HSC secrete 21 stellakines that are predicted to act primarily on endothelial and immune cells based on their receptor expression (Figure 6B). As such, mRNA expression of the receptors for *WNT4*, *NTN1*, *EFNB1*, *BMP5*, *GDF2*, *GDF10* and *SEMA3C* was largely restricted to endothelial cells, while the cellular targets for *CCL2*, *CCL11*, *CXCL10*, *CXCL12*, *CXCL16*, *CTGF* and *GAS6* were primarily immune cells, such as macrophage, DC, T and B cells. Whole liver RNA-seq analysis indicated that the expression of many of these HSC-derived ligands was elevated in NASH and associated with liver injury (Figure 6C and S6A), suggesting that increased stellakine secretion and action are linked to diet-induced NASH pathogenesis.

The HSC-enriched receptors (27) can be divided into three broad categories based on their known biological functions: ECM biology and fibrosis, cytokine signaling and vasoactive receptors (Figure 6D). A number of HSC receptors have been implicated in liver fibrosis, including *Pdgfrb*, *Fgfr2*, *Ddr2*, *Ryk* and *Lrp1*. For example, Discoidin domain receptor 2 (*Ddr2*) serves as a non-integrin collagen receptor that regulates HSC activation, ECM deposition and liver fibrosis (Leitinger, 2014). Interestingly, mRNA expression of many of these HSC receptors was altered in NASH livers (Figure S6B). We observed restricted HSC expression of p75 neurotrophin receptor (*Ngfr*), which promotes HSC apoptosis in response to Nerve growth factor (NGF) (Trim et al., 2000). Importantly, our scRNA-seq analysis revealed cholangiocytes and HSC as two major sources of NGF, supporting a dual paracrine

and autocrine mechanism in mediating NGF-induced HSC cell death. Together, these results demonstrate that HSC are uniquely equipped to respond to diverse extracellular signals and serve as a hub for intrahepatic signaling by secreting stellakines.

### Vasoactive hormone signaling in HSC

HSC are known to harbor contractile apparatus and undergo contraction and relaxation to modulate liver sinusoidal blood flow (Friedman, 2008; Reynaert et al., 2008). We uncovered a surprisingly diverse set of vasoactive hormone-responsive receptors on HSC. Compared to other cell types, HSC exhibited enriched mRNA expression for Endothelin receptor type a (Ednra), Ednrb, Angiotensin II receptor type 1a (Agtr1a) and Adrenergic receptor  $\alpha$  2b (Adra2b), which promote HSC constriction upon activation (Reynaert et al., 2008). mRNA transcripts for several GPCRs targeted by vasorelaxation peptide hormones were also abundantly expressed by HSC, including Ramp1, Calcl1, Pth1r and Vipr1. Ramp1 and Calcl1 together form a receptor for Calcitonin gene-related peptide, a vasodilator, while PTH1R and VIPR1 are receptors for parathyroid hormone (PTH)/parathyroid hormone-related protein (PTHrP) and vasoactive intestinal peptide (VIP)/pituitary adenylate cyclase-activating peptide (PACAP), respectively. Importantly, HSC-enriched expression for Ednrb, Adra2b, Vipr1, Pth1r and Ramp1 was observed in both mice and humans (Figure 6E), illustrating likely functional conservation of vasoactive hormone signaling in HSC.

We confirmed VIPR1 protein expression in HSC using double immunofluorescence staining. As shown in Figure 6F, VIPR1-positive cells were also positive for Decorin (DCN), a collagen-binding protein produced by Desmin-positive HSC (Meyer et al., 1992). To confirm that these vasoactive receptors are functional in contractile signaling, we performed treatments on cultured mouse and human HSC. Activation of endothelin receptors and Agtr1a with their respective ligands (Endothelin 1, ET-1 and Angiotensin II, Ang II) triggered a rapid and robust increase of intracellular calcium levels in cultured primary mouse HSC (Figure 7A). Importantly, ET-1 and Ang II also potently stimulated the calcium response in primary human HSC (Figure 7B). The ability of ET-1 and Ang II to raise intracellular calcium was greatly diminished in the presence of PACAP, a physiological ligand of VIPR1 that promotes smooth muscle relaxation and gastrointestinal motility (Makhlouf and Murthy, 1997). Immunoblotting analysis using antibodies recognizing phosphorylated protein kinase A (p-PKA) substrates showed that PACAP induced robust PKA signaling, likely as a result of increased cAMP production in response to GPCR activation (Figure 7C and S6C). qPCR analysis revealed that hepatic Vipr1 mRNA expression was significantly reduced by NASH and negatively correlated with Col1a1 gene expression (Figure S6D–E). These functional studies demonstrate that HSC contraction and relaxation are likely balanced by the opposing action of physiological hormones. Surprisingly, we did not detect significant expression of Vip, Pacap, Pth and Pthrp transcripts in our scRNA-seq dataset, suggesting that their receptors likely respond to ligands of endocrine and/or neuroendocrine origins.

### Regulation of stellakine gene expression by autocrine IL11 signaling

Expression of several receptors for the IL-6 family of cytokines was notable in the HSC cluster, including Lifr, Il11ra1 and Il6st; the latter encodes gp130, a signaling receptor

shared by this family of cytokines (Sims and Walsh, 2010). Our analysis indicated that *Il11ra1* mRNA expression was most abundant in HSC (Figure S7A). *Il11ra1* encodes a co-receptor for IL11 and mediates IL11 signaling through gp130. To determine whether IL11 signaling may be altered during NASH, we analyzed hepatic *Il11* mRNA expression in two models of diet-induced NASH. Interestingly, both AMLN diet and CDAHFD feeding robustly induced *Il11* expression in mouse liver, coinciding with NASH pathogenesis (Figure 7D). We surveyed the source of *Il11* expression and found that HSC displayed the highest mRNA expression among ten major liver cell types (Figure S7A). These results suggest that autocrine IL11 signaling may be augmented during NASH when HSC assume a more activated phenotype. In support of this, we found that TGF $\beta$  strongly stimulated *Il11* mRNA expression in immortalized mouse HSC (Figure 7E).

IL11 has been previously implicated in cardiac fibrosis (Obana et al., 2010; Schafer et al., 2017); however, its pathophysiological role and mechanism of action remain to be fully ascertained. To explore how IL11 signaling regulates HSC biology, we treated cultured mouse HSC with vehicle, TGF $\beta$  or IL11 and analyzed expression of genes involved in fibrosis. As expected, TGF $\beta$  treatment potently induced mRNA expression of *Col1a1*, *Acta2* and *Ctgf*, known targets of TGF $\beta$  signaling and HSC activation (Figure 7F). While IL11 robustly induced mRNA expression of *Sox3*, a target of cytokine signaling mediated by STAT3 activation, it failed to increase fibrosis gene expression in HSC. Instead, IL11 treatment stimulated the expression of a subset of stellakines including *Cxcl1*, *Wnt4* and *Ccl11*, all of which exhibit increased expression in the liver in two models of diet-induced NASH (Figure 7G and S7B). The expression of *Cxcl10* and *Ntn1* remained largely unaltered in HSC treated with IL11, suggesting that they are likely regulated by other upstream signals. We next explored the signaling pathways that mediate IL11 induction of stellakine gene expression. IL11 treatment resulted in a rapid and robust increase in ERK and STAT3 phosphorylation (Figure 7H). Remarkably, inhibition of STAT3 activation by Stattic essentially abolished the induction of *Cxcl1*, *Wnt4* and *Ccl11* in response to IL11 (Figure 7I). In contrast, inhibition of ERK activation by U0126 failed to elicit similar effects. Together, these results illustrate a prominent role of autocrine IL11 signaling in HSC in the control of stellakine gene expression (Figure 7J).

## Discussion

The mammalian tissues harbor diverse cell types that exhibit distinct molecular signatures and functional properties. While intercellular crosstalk has been recognized as a fundamental feature of tissue biology, the precise nature of these signaling modalities remains obscure due to limited cellular resolution of bulk transcriptomic and proteomic analyses. Using scRNA-seq based secretome analysis, we mapped the transcriptional landscape of secreted ligands and membrane receptors in major liver cell populations and constructed a ligand-receptor network that governs extensive autocrine and paracrine crosstalk in the liver. A notable advantage of single-cell transcriptome analysis is the unprecedented accuracy in delineating the cellular sources of secreted ligands and their potential target cell types. Beyond intrahepatic crosstalk via secreted factors, we observed abundant expression of endocrine and neuroendocrine receptors on liver NPC, such as endothelial cells and HSC, suggesting that extrahepatic ligands may serve an important role

in shaping the biology of diverse cell types in the liver. Together, this work reveals a global map of secretome gene expression in the liver at single-cell resolution and provides a blueprint for deconstructing the dynamic nature of intercellular crosstalk in homeostasis and disease.

Comparative single-cell analysis of NPC from healthy and NASH livers revealed profound disruptions of the vascular and angiocrine signaling network. It is important to note that these disruptions of the cell-cell signaling network in the liver appear to be conserved pathophysiological features of NASH in both mice and humans. Unexpectedly, we observed a NASH-specific macrophage population that is marked by high levels of expression of Trem2. This unique hepatic macrophage population is analogous to the Trem2-positive microglial cells found in Alzheimer's Disease (Keren-Shaul et al., 2017), a neurodegenerative disorder causally linked to aberrant function of tissue-resident macrophages. To date, Trem2 mutations have been linked to Alzheimer's Disease, Nasu-Hakola disease, frontotemporal lobar degeneration, ALS and Parkinson's disease (Lill et al., 2015), suggesting Trem2 has a critical role in resident macrophage function in disease. While the precise mechanism through which Trem2 regulates disease pathogenesis in the brain remains poorly understood, several *in vivo* studies have begun to elucidate the importance of the Trem2-positive macrophage population. Of note, Trem2 deficiency in mice results in failure of microglia to proliferate and cluster around  $\alpha\beta$  plaques in a mouse model for Alzheimer's Disease (Wang et al., 2015). Overexpression of Trem2 *in vitro* has been found to increase microglial capacity for phagocytosis of apoptotic neurons and  $\alpha\beta$  plaques (Jiang et al., 2014). These findings strongly suggest a role for NAM in the clearance of apoptotic and lipid-laden hepatocytes in the NASH liver. In support of this, a recent study has shown that Trem2-deficient mice developed more severe immune-mediated liver injury (Perugorria et al., 2018). As such, the emergence of Trem2-positive macrophages likely serves an adaptive and protective role during diet-induced NASH.

A notable aspect of the HSC secretome is its dual role as a source of the ECM structural and remodeling proteins and diverse signaling ligands. The list of stellakines becomes even longer with a less stringent UMI cutoff, underscoring the prominent role of HSC as a signaling hub in the liver. Ligand receptor connectivity analysis of the stellakine signaling network highlights endothelial and immune cells as the primary cellular targets of stellakine action. These findings are consistent with the ability of HSC to engage immune cells and orchestrate tissue injury response and repair (Friedman, 2008). As expression of many stellakines is induced during NASH, it is likely that they may contribute to both adaptive and maladaptive HSC reprogramming in the context of chronic liver injury. The induction of stellakine expression is at least in part attributed to the IL11/IL11Ra autocrine signaling loop driven by TGF $\beta$  signaling in HSC. While the pathophysiological role of autocrine IL11 signaling remains unknown, our results strongly suggest that the dysregulations of stellakine secretion likely represent a key aspect of HSC biology during NASH pathogenesis.

A rather unexpected finding from the single-cell membrane receptor mapping is the identification of several GPCRs that respond to vasoactive hormones. For example, angiotensin and endothelin receptors are known to respond to Angiotensin and Endothelin 1, respectively, to trigger calcium response and contraction of smooth muscle cells. Similarly,

activation of the  $\alpha_2$  adrenergic receptor promotes vasoconstriction. In contrast, several GPCRs responsive to vasorelaxing peptides including Pth1r, Vipr1, Ramp1, Ramp2 and Calcrl are also highly expressed on HSC. Importantly, our functional studies indicate that these vasoactive GPCRs are highly potent in triggering intracellular calcium responses, a prerequisite for cellular contractile activities. These results strongly support the notion that HSC are capable of responding to diverse vasoactive hormones and likely play an important role in the control of intrahepatic vascular tone (Hellerbrand, 2013; Reynaert et al., 2008). Future work is needed to delineate the physiological role of vasoactive signaling in HSC in the control of hepatic blood flow and its potential contribution to the pathogenesis of portal hypertension.

While this work delineates the landscape of liver cell secretome gene expression and NASH-associated reprogramming, several key predictions require further functional validation. For example, it remains to be established whether hepatic vascular dysfunctions serve as a pathogenic factor that is causally linked to NASH progression. The emergence of TREM2-positive NAM in both mouse and human NASH is particularly intriguing. Future work is needed to establish the mechanisms underlying the induction of this unique macrophage population in NASH and how NAM contributes to tissue homeostasis in healthy and disease states. Finally, whether HSC functions as a gatekeeper of hepatic metabolism via the regulation of its contractility remains an important unanswered question. Nevertheless, our work provides strong support for the concept that non-parenchymal cell types in metabolic tissues play a more pervasive role in metabolic control and disease progression.

## STAR METHODS

Detailed methods are provided in the online version of this paper and include the following:

### LEAD CONTACT AND MATERIALS AVAILABILITY

Further information and requests for resources and reagents should be directed to and will be fulfilled by the Lead Contact, Jiandie Lin (jdlin@umich.edu). This study did not generate new unique reagents.

### EXPERIMENTAL MODEL AND SUBJECT DETAILS

**Human NASH study**—The study population consisted of 144 Mexican mestizo subjects (male and female) who underwent bariatric surgery for morbid obesity. A total of 82.6% were female and the mean age of the participants was  $38.6 \pm 10.1$  years. Detailed characteristics of the study have been reported elsewhere (Gutierrez-Vidal et al., 2015; Leon-Mimila et al., 2015; Vega-Badillo et al., 2016). Liver biopsies were collected in RNAlater (Sigma, St. Louis, MO) during surgery and processed for RNA sequencing analyses as describe previously (Hui et al., 2018). This study was performed according to the principles of the Declaration of Helsinki and was approved by the institutional review boards of the National Institute of Genomic Medicine (Mexico) and the Hospital Dr. General Ruben Leñero. All participants provided written informed consent prior to their inclusion. Correlations of normalized values of RNA sequencing data with transaminase levels, steatosis, ballooning, inflammation and NAS score were evaluated using partial correlations

adjusting for batch, age, sex, BMI and T2D status. The differences between groups were evaluated using ANCOVA adjusting for batch, age, sex, BMI and T2D status. Because transaminase levels were not normally distributed, the values were log transformed before performing statistical analyses.

**Mice**—All animal studies were performed following procedures approved by the Institutional Animal Care & Use Committee at the University of Michigan. Mice were housed in pathogen-free facilities under 12-h light-dark cycles with free access to food and water. For standard chow feeding, mice were fed Teklad 5001 Laboratory Diet. For AMLN diet-induced NASH, C57/B16 mice were fed a diet containing 40% fat (of which 18% was trans-fat), 22% fructose, and 2% cholesterol (D09100301, Research Diets Inc.) for 20 weeks, as previously described (Clapper et al., 2013; Guo et al., 2017). In a separate diet-induced NASH model, C57/B16 mice were maintained on Choline-Deficient, Amino acid-defined HFD (45 kcal% fat) containing 0.1% methionine (CDAHFD, A06071309, Research Diets Inc.) for 6 weeks. In Elafibranor treated groups, C57/B16 mice were placed on CDAHFD and gavaged daily with 10mg Elafibranor/kg body weight in 1% CMC or vehicle for 24 days.

**Primary HSC isolation and cell lines**—Mouse HSC were isolated from mouse livers by pronase/collagenase digestion followed by gradient centrifugation, as recently described (Mederacke et al., 2015). Briefly, NPC suspension was placed at the bottom of a four-layer OptiPrep gradient (1.034, 1.043, 1.058 and 1.085g/ml) and centrifuged at 1,500g for 30 min with the brake off. HSC were collected from the interface between two top layers (1.034 and 1.043g/ml) and cultured in DMEM containing 20% fetal bovine serum (FBS). Human HSC were purchased from ScienCell Research Laboratories and maintained in commercial HSC medium (ScienCell Research Laboratories, #5301). For immortalization of mouse HSC, isolated primary HSC were transduced with a recombinant retroviral vector expressing SV40 large T-antigen, followed by selection with G418. Immortalized HSC were maintained in DMEM containing 10% FBS.

## METHOD DETAILS

**RNA extraction and analysis**—Total RNA was extracted from frozen livers or harvested cells using Trizol (Alkali Scientific, TRZ-100). Quantitative RT-PCR gene expression analysis was performed as previously described (Guo et al., 2017; Wang et al., 2014). Liver RNA sequencing was performed using Illumina HiSeq 4000 at the University of Michigan DNA Sequencing Core. A list of qPCR primers is listed in Supplementary Table S7.

**Quantitative proteomic analysis**—TMT experiments were performed as previously described (Zhao et al., 2017). Briefly, proteins were extracted from three pairs of chow and AMLN livers, reduced with 2 mM DTT for 10 min and alkylated with 50 mM iodoacetamide for 30 min in dark. Proteins were digested by Lys-C (Wako, at a 1:100 enzyme/protein ratio) for 2 hrs at RT followed by overnight digestion with trypsin (Thermo Fisher Scientific, at 1:100 enzyme/protein ratio). Peptides were desalted with Oasis HLB cartridges (Waters), resuspended in 200 mM HEPES (pH 8.5) to a final concentration of 1 µg/µL, and labeled with amine-based TMT six-plex reagents (Thermo Fisher Scientific).



Three replicate samples were prepared for the control samples (TMT-126, -127 and -128), and the NASH samples (TMT-129, -130 and -131), respectively.

Samples were desalted and fractionated by bRPLC (basic pH reversed phase HPLC) on a ZORBAX 300 Extend-C18 column (Narrow Bore RR 2.1 mm x 100 mm, 3.5  $\mu$ m particle size, 300  $\text{\AA}$  pore size). Seventeen fractions were collected, which were lyophilized, desalted and analyzed by LC-MS/MS on a Thermo Orbitrap Elite mass spectrometer using a top 15 HCD method. MS/MS spectra were searched against a composite database of the mouse UniProt protein database and its reversed complement using the Sequest (Rev28) algorithm. Search parameters allowed for a static modification of 57.02146 Da on cystine (Carbamidomethyl), a variable modification of 15.994915 Da on methionine (oxidation), and a static modification of TMT labels (229.16293 Da) on peptide N-terminus and lysine. For TMT quantification, a 0.03 Th window was scanned around the theoretical m/z of each reporter ion (126:126.127725; 127:127.124760; 128:128.134433; 129:129.131468; 130:130.141141; 131:131.138176). The maximum intensity of each reporter ion was extracted, which was converted to signal-to-noise (S/N) ratios.

**Isolation and scRNA-seq analysis of liver NPC**—Liver NPC were isolated following a two-step protocol of pronase/collagenase digestion (Mederacke et al., 2015). Briefly, the liver was perfused in situ with calcium-free Hank's Balanced Salt Solution (HBSS) containing 0.2mg/ml EDTA, followed by sequential perfusion with 0.4mg/ml pronase (Sigma, P5147) and 0.2% collagenase type II (Worthington, LS004196). The liver was minced and further digested with HBSS containing 0.2% collagenase type II, 0.4 mg/ml pronase and 0.1mg/ml DNase I (Roche, R104159001) in 37 °C water bath with shaking for 20 min. Digestion was terminated with DMEM containing 10% serum. The resulting liver cell suspension was centrifuged at 50g for 3 min to remove hepatocytes and passed through 30 $\mu$ m nylon cell strainer followed by treatment with 0.8% NH<sub>4</sub>Cl to lyse red blood cells. This NPC suspension was centrifuged, resuspended in HBSS, and subjected to density gradient centrifugation using 20% Optiprep (Axis Shield, 1114542) to remove dead cells. Cell viability was confirmed by trypan blue exclusion. The resulting NPC were subjected to scRNA-seq analysis using 10X Genomics Chromium Single-Cell 3' according to the manufacturer's instructions.

**LSEC RNA sequencing**—LSEC were isolated from chow and AMLN mouse livers as previously described (Meyer et al., 2016). A combination of negative depletion with CD11b magnetic beads followed by positive-selection with CD146 magnetic beads was used to isolate LSEC from liver NPC suspension. Total RNA was isolated from purified LSEC for RNA sequencing (Beijing Genomics Institute, China). Twenty million reads were obtained using a paired-end 50bp module on BGISEq-500.

**Flow cytometry**—Flow cytometry analysis of sinusoidal endothelial cells was performed as we previously described (Ji et al., 2014; Ji et al., 2012). Briefly, hepatic NPC were collected as previously described. The isolated cells were centrifuged at 1,000 rpm for 5 min. The cells were washed and re-suspended in cold staining buffer, followed by incubation with anti-CD16/CD32 antibody to block Fc receptors. For hepatic macrophages, liver samples were filtered through 100  $\mu$ m strainers in 1% BSA in PBS and centrifuged at 50x g

for 3 minutes to remove hepatocytes. NPC were harvested as intermediate fraction following gradient centrifugation in 25% optiprep at 1500x g for 20 minutes. After wash,  $1 \times 10^6$  cells were incubated with 100  $\mu$ l of various antibodies diluted at optimal concentrations for 20 min at 4 °C. The fluorochrome-conjugated antibodies against CD45 (30-F1; Biolegend, 103130), CD146 (ME-9F1; Biolegend, 134711), CD36 (HM36; Biolegend, 102605), CD45 (I3/2.3; Biolegend, 147716), F4/80 (BM8; Biolegend, 123114), CD11b (M1/80; Biolegend, 101226), CD9 (MZ3; Biolegend, 124805), GPNMB (CSTREVL; Thermo Fisher, 50-5708-82), and CXCL9 (MIG-2F5.5; Biolegend, 515603), avidin-PerCP (Biolegend, 103130) were used. LSEC were gated as CD45-CD146+ cells, liver macrophages were gated as CD45+F4/80<sup>hi</sup>CD11b<sup>int</sup> or CD45+F4/80<sup>int</sup>CD11b<sup>hi</sup> for KC or MDM, respectively. For intracellular staining, the cells were fixed and permeabilized by BD Cytotfix/Cytoperm Fixation/Permeabilization Kit per manufacturer's protocol. Samples were analyzed using BD LSR cell analyzer at the Vision Research Core Facility at the University of Michigan Medical School. Data were analyzed using the CellQuest software (BD Biosciences) and Flowjo ([Flowjo.com](http://Flowjo.com)).

**Calcium imaging**—The HSC cultures used for intracellular calcium imaging were within five passages following isolation. For calcium imaging, cells were seeded on cover glasses 2 days before loading with calcium indicator FURA-2AM (Thermo Fisher, F1201) and imaged with an inverted fluorescent microscope. Images were acquired every other second to monitor the dynamic changes in intracellular calcium levels in response to 100 nM ET-1 or Ang II alone or in combination with 100 nM PACAP.

**Immunofluorescence staining**—Liver tissues were fixed in situ with 4% paraformaldehyde, incubated with 30% sucrose in PBS overnight, and embedded in OCT. Frozen sections were permeabilized with 0.3% Triton X-100 in PBS and then blocked in 5% BSA, followed by incubation in primary antibody solution overnight at 4 °C, and subsequently in secondary antibody solution at room temperature for one hour. Sections were mounted in VECTASHIELD Antifade Mounting Medium (Vector Laboratories, H-1000). Images were taken with Olympus fluorescence microscope.

**Western Blot Analysis**—Total liver protein extracts and cell lysates were prepared using a lysis buffer containing 50 mM Tris-HCl (pH = 7.5), 137 mM NaCl, 1 mM EDTA, 1% Triton X-100, 10% glycerol, 10 mM NaF, 10 mM Na<sub>4</sub>P<sub>2</sub>O<sub>7</sub>, 1 mM Na<sub>3</sub>VO<sub>4</sub>, and protease inhibitor cocktail. The lysates were separated by SDS-PAGE and transferred to a PVDF membrane, followed by immunoblotting with primary antibodies and secondary antibodies.

## QUANTIFICATION AND STATISTICAL ANALYSIS

**Data analysis**—For total liver and LSEC RNA-seq, sequence reads were mapped to mouse genome mm10 using STAR. HTSeq was used to count the sequences that can be mapped to gene features. The raw read counts were normalized and processed for differential expression gene analysis using DESeq2. The significant expressed genes were determined by FDR less than 0.05.

For scRNA-seq, a total of 39,575 single cell NPC isolated from three chow and three NASH mice were processed using 10X Genomics CHROMIUM Single Cell 3' Solution. The libraries were sequenced using Illumina NextSeq High-Output, HiSeq 4000 and NovaSeq. We obtained a total of over 1.7 billion reads with an average of 43,122 reads per cell. Approximately 55.4% of the sequence reads can be confidently mapped to the mouse transcriptome. Seurat package (version 2.3.4) was used to analyze single cell RNA-seq data (Butler et al., 2018). After removing doublets and cells with low quality, 33,168 cells that expressed more than 500 genes and 19,349 genes with transcripts detected in more than 3 cells were used for further analysis. Unique sequencing reads for each gene were normalized to total Unique Molecular Identifiers (UMIs) in each cell to obtain normalized UMI values. The top 1,000 highly variable genes were used for canonical correlation analysis (CCA) implemented in Seurat. Unsupervised clustering was applied after aligning the top 25 dimensions resulted from the CCA using a resolution of 0.07. The identity for each cluster was assigned based on the prior knowledge of marker genes. A higher resolution parameter was applied for sub-clustering of the endothelial and myeloid clusters. The t-SNE plots, violin plots, bar plots, circular plot, bubble plots, feature plots and heatmaps were generated by R and Java TreeView. Dot plot was generated using GraphPad.

**Mouse secretome and network visualization**—The mouse secretome database was compiled using gene lists obtained from Secreted Protein Database (SPD: <http://spd.cbi.pku.edu.cn>) (Chen et al., 2005) and IUPHAR database (<http://www.iuphar-db.org/index.jsp>), and manually curated to improve accuracy of gene annotation. Members of the solute carrier protein superfamily were not included in the current version. The secretome genes with normalized UMI values > 1.0 in any of the liver cell clusters were selected for construction of intrahepatic ligand-receptor signaling network. Ligand and receptor pairing dataset was obtained from Fantom5 (<http://fantom.gsc.riken.jp>), as recently described (Ramilowski et al., 2015). Network connectivity was visualized using Gephi graph tool (<https://gephi.org>).

**Macrophage polarization index (MPI)**—Macrophage polarization index was generated based on scRNA-seq profiles of polarized bone marrow-derived macrophages following LPS/cytokine stimulation (Li et al., 2019). Comparing M1 (LPS+IFN $\gamma$  stimulation) and M2 (IL4+IL13 stimulation) profiles, gene with most significant changes were selected to calculate similarities of each cells to the whole population of M1 or M2 states. A linear regression line of all scRNA-seq profiles was generated and terms as “polarization axis” (<https://macspectrum.uconn.edu>). The projection of each cell on this axis was indexed as macrophage polarization index (MPI): higher MPI suggesting more “M1-like” (more inflammatory) states with lower MPI suggesting more “M2-like” (less inflammatory) states.

## DATA AND CODE AVAILABILITY

All RNA-seq data generated in this work have been deposited into the Gene Expression Omnibus (GEO) database (GSE119340, GSE129516). Raw western blot images found at Mendeley link (<http://dx.doi.org/10.17632/4dmtjj97m8.1>).

## Supplementary Material

Refer to Web version on PubMed Central for supplementary material.

## Acknowledgements

We thank Drs. Mark Coggeshall and Glenn Dorsam for their generosity in sharing anti-VIPR1 and anti-FCGR2B antibodies, respectively. We thank Dr. Luis Macias-Kauffer for the analyses of RNA-seq data in humans. This work was supported in part by NIH (DK102456, DK112800 and DK118731 to J.L. and GM114160 and GM122932 to Y.Y.), and a pilot grant from the Michigan Diabetes Research Center (DK020572), Welch Foundation (I-1800 to Y.Y.) and the UCLA Clinical and Intramural Award: UL1TR001881 (A.J.L. and A.H.V.). H.K. was supported by an NRSA fellowship (FDK117615) and MSTP training grant (T32GM007863). T.L. was supported by Patten Predoctoral Fellowship provided by the University of Michigan.

## References

- Arendt BM, Comelli EM, Ma DW, Lou W, Teterina A, Kim T, Fung SK, Wong DK, McGilvray I, Fischer SE, et al. (2015). Altered hepatic gene expression in nonalcoholic fatty liver disease is associated with lower hepatic n-3 and n-6 polyunsaturated fatty acids. *Hepatology* 61, 1565–1578. [PubMed: 25581263]
- Butler A, Hoffman P, Smibert P, Papalexi E, and Satija R (2018). Integrating single-cell transcriptomic data across different conditions, technologies, and species. *Nat Biotechnol* 36, 411–420. [PubMed: 29608179]
- Chen Y, Zhang Y, Yin Y, Gao G, Li S, Jiang Y, Gu X, and Luo J (2005). SPD--a web-based secreted protein database. *Nucleic Acids Res* 33, D169–173. [PubMed: 15608170]
- Clapper JR, Hendricks MD, Gu G, Wittmer C, Dolman CS, Herich J, Athanacio J, Villescaz C, Ghosh SS, Heilig JS, et al. (2013). Diet-induced mouse model of fatty liver disease and nonalcoholic steatohepatitis reflecting clinical disease progression and methods of assessment. *Am J Physiol Gastrointest Liver Physiol* 305, G483–495. [PubMed: 23886860]
- Cohen JC, Horton JD, and Hobbs HH (2011). Human fatty liver disease: old questions and new insights. *Science* 332, 1519–1523. [PubMed: 21700865]
- Deczkowska A, Keren-Shaul H, Weiner A, Colonna M, Schwartz M, and Amit I (2018). Disease-Associated Microglia: A Universal Immune Sensor of Neurodegeneration. *Cell* 173, 1073–1081. [PubMed: 29775591]
- Diehl AM, and Day C (2017). Cause, Pathogenesis, and Treatment of Nonalcoholic Steatohepatitis. *N Engl J Med* 377, 2063–2072. [PubMed: 29166236]
- Friedman SL (2008). Hepatic stellate cells: protean, multifunctional, and enigmatic cells of the liver. *Physiol Rev* 88, 125–172. [PubMed: 18195085]
- Gawad C, Koh W, and Quake SR (2016). Single-cell genome sequencing: current state of the science. *Nat Rev Genet* 17, 175–188. [PubMed: 26806412]
- Geven C, Kox M, and Pickkers P (2018). Adrenomedullin and Adrenomedullin-Targeted Therapy As Treatment Strategies Relevant for Sepsis. *Front Immunol* 9, 292. [PubMed: 29520277]
- Guo L, Zhang P, Chen Z, Xia H, Li S, Zhang Y, Kobberup S, Zou W, and Lin JD (2017). Hepatic neuregulin 4 signaling defines an endocrine checkpoint for steatosis-to-NASH progression. *J Clin Invest* 127, 4449–4461. [PubMed: 29106384]
- Gutierrez-Vidal R, Vega-Badillo J, Reyes-Fermin LM, Hernandez-Perez HA, Sanchez-Munoz F, Lopez-Alvarez GS, Larrieta-Carrasco E, Fernandez-Silva I, Mendez-Sanchez N, Tovar AR, et al. (2015). SFRP5 hepatic expression is associated with non-alcoholic liver disease in morbidly obese women. *Ann Hepatol* 14, 666–674. [PubMed: 26256895]
- Halpern KB, Shenhav R, Massalha H, Toth B, Egozi A, Massasa EE, Medgalia C, David E, Giladi A, Moor AE, et al. (2018). Paired-cell sequencing enables spatial gene expression mapping of liver endothelial cells. *Nat Biotechnol* 36, 962–970. [PubMed: 30222169]
- Halpern KB, Shenhav R, Matcovitch-Natan O, Toth B, Lemze D, Golan M, Massasa EE, Baydatch S, Landen S, Moor AE, et al. (2017). Single-cell spatial reconstruction reveals global division of labour in the mammalian liver. *Nature* 542, 352–356. [PubMed: 28166538]

- Han X, Wang R, Zhou Y, Fei L, Sun H, Lai S, Saadatpour A, Zhou Z, Chen H, Ye F, et al. (2018). Mapping the Mouse Cell Atlas by Microwell-Seq. *Cell* 172, 1091–1107 e1017. [PubMed: 29474909]
- Hellerbrand C (2013). Hepatic stellate cells--the pericytes in the liver. *Pflugers Arch* 465, 775–778. [PubMed: 23292551]
- Hui ST, Kurt Z, Tuominen I, Norheim F, R CD, Pan C, Dirks DL, Magyar CE, French SW, Chella Krishnan K, et al. (2018). The Genetic Architecture of Diet-Induced Hepatic Fibrosis in Mice. *Hepatology* 68, 2182–2196. [PubMed: 29907965]
- Ji Y, Sun S, Goodrich JK, Kim H, Poole AC, Duhamel GE, Ley RE, and Qi L (2014). Diet-induced alterations in gut microflora contribute to lethal pulmonary damage in TLR2/TLR4-deficient mice. *Cell Rep* 8, 137–149. [PubMed: 24953658]
- Ji Y, Sun S, Xia S, Yang L, Li X, and Qi L (2012). Short term high fat diet challenge promotes alternative macrophage polarization in adipose tissue via natural killer T cells and interleukin-4. *J Biol Chem* 287, 24378–24386. [PubMed: 22645141]
- Jiang T, Tan L, Zhu XC, Zhang QQ, Cao L, Tan MS, Gu LZ, Wang HF, Ding ZZ, Zhang YD, et al. (2014). Upregulation of TREM2 ameliorates neuropathology and rescues spatial cognitive impairment in a transgenic mouse model of Alzheimer's disease. *Neuropsychopharmacology* 39, 2949–2962. [PubMed: 25047746]
- Keren-Shaul H, Spinrad A, Weiner A, Matcovitch-Natan O, Dvir-Szternfeld R, Ulland TK, David E, Baruch K, Lara-Astaiso D, Toth B, et al. (2017). A Unique Microglia Type Associated with Restricting Development of Alzheimer's Disease. *Cell* 169, 1276–1290 e1217. [PubMed: 28602351]
- Krenkel O, Puengel T, Govaere O, Abdallah AT, Mossanen JC, Kohlhepp M, Liepelt A, Lefebvre E, Luedde T, Hellerbrand C, et al. (2018). Therapeutic inhibition of inflammatory monocyte recruitment reduces steatohepatitis and liver fibrosis. *Hepatology* 67, 1270–1283. [PubMed: 28940700]
- Krenkel O, and Tacke F (2017). Liver macrophages in tissue homeostasis and disease. *Nat Rev Immunol* 17, 306–321. [PubMed: 28317925]
- Leitinger B (2014). Discoidin domain receptor functions in physiological and pathological conditions. *Int Rev Cell Mol Biol* 310, 39–87. [PubMed: 24725424]
- Leon-Mimila P, Vega-Badillo J, Gutierrez-Vidal R, Villamil-Ramirez H, Villareal-Molina T, Larrieta-Carrasco E, Lopez-Contreras BE, Kauffer LR, Maldonado-Pintado DG, Mendez-Sanchez N, et al. (2015). A genetic risk score is associated with hepatic triglyceride content and non-alcoholic steatohepatitis in Mexicans with morbid obesity. *Exp Mol Pathol* 98, 178–183. [PubMed: 25597287]
- Li C, Menoret A, Farragher C, Ouyang Z, Bonin C, Holvoet P, Vella AT, and Zhou B (2019). Single cell transcriptomics based-MacSpectrum reveals novel macrophage activation signatures in diseases. *JCI Insight* 5.
- Lill CM, Rengmark A, Pihlstrom L, Fogh I, Shatunov A, Sleiman PM, Wang LS, Liu T, Lassen CF, Meissner E, et al. (2015). The role of TREM2 R47H as a risk factor for Alzheimer's disease, frontotemporal lobar degeneration, amyotrophic lateral sclerosis, and Parkinson's disease. *Alzheimers Dement* 11, 1407–1416. [PubMed: 25936935]
- MacParland SA, Liu JC, Ma XZ, Innes BT, Bartczak AM, Gage BK, Manuel J, Khuu N, Echeverri J, Linares I, et al. (2018). Single cell RNA sequencing of human liver reveals distinct intrahepatic macrophage populations. *Nat Commun* 9, 4383. [PubMed: 30348985]
- Makhlouf GM, and Murthy KS (1997). Signal transduction in gastrointestinal smooth muscle. *Cell Signal* 9, 269–276. [PubMed: 9218127]
- Matsumoto M, Hada N, Sakamaki Y, Uno A, Shiga T, Tanaka C, Ito T, Katsume A, and Sudoh M (2013). An improved mouse model that rapidly develops fibrosis in non-alcoholic steatohepatitis. *Int J Exp Pathol* 94, 93–103. [PubMed: 23305254]
- Mederacke I, Dapito DH, Affo S, Uchinami H, and Schwabe RF (2015). High-yield and high-purity isolation of hepatic stellate cells from normal and fibrotic mouse livers. *Nat Protoc* 10, 305–315. [PubMed: 25612230]



- Meex RCR, and Watt MJ (2017). Hepatokines: linking nonalcoholic fatty liver disease and insulin resistance. *Nat Rev Endocrinol* 13, 509–520. [PubMed: 28621339]
- Meyer DH, Krull N, Dreher KL, and Gressner AM (1992). Biglycan and decorin gene expression in normal and fibrotic rat liver: cellular localization and regulatory factors. *Hepatology* 16, 204–216. [PubMed: 1618472]
- Meyer J, Lacotte S, Morel P, Gonelle-Gispert C, and Buhler L (2016). An optimized method for mouse liver sinusoidal endothelial cell isolation. *Exp Cell Res* 349, 291–301. [PubMed: 27815020]
- Obana M, Maeda M, Takeda K, Hayama A, Mohri T, Yamashita T, Nakaoka Y, Komuro I, Takeda K, Matsumiya G, et al. (2010). Therapeutic activation of signal transducer and activator of transcription 3 by interleukin-11 ameliorates cardiac fibrosis after myocardial infarction. *Circulation* 121, 684–691. [PubMed: 20100971]
- Pais R, Barritt A.S.t., Calmus Y, Scatton O, Runge T, Lebray P, Poynard T, Ratziu V, and Conti F (2016). NAFLD and liver transplantation: Current burden and expected challenges. *J Hepatol* 65, 1245–1257. [PubMed: 27486010]
- Perugorria MJ, Esparza-Baquer A, Oakley F, Labiano I, Korosec A, Jais A, Mann J, Tiniakos D, Santos-Laso A, Arbelaz A, et al. (2018). Non-parenchymal TREM-2 protects the liver from immune-mediated hepatocellular damage. *Gut*.
- Poisson J, Lemoine S, Boulanger C, Durand F, Moreau R, Valla D, and Rautou PE (2017). Liver sinusoidal endothelial cells: Physiology and role in liver diseases. *J Hepatol* 66, 212–227. [PubMed: 27423426]
- Rafii S, Butler JM, and Ding BS (2016). Angiocrine functions of organ-specific endothelial cells. *Nature* 529, 316–325. [PubMed: 26791722]
- Ramilowski JA, Goldberg T, Harshbarger J, Kloppmann E, Lizio M, Satagopam VP, Itoh M, Kawaji H, Carninci P, Rost B, et al. (2015). A draft network of ligand-receptor-mediated multicellular signalling in human. *Nat Commun* 6, 7866. [PubMed: 26198319]
- Regev A, Teichmann SA, Lander ES, Amit I, Benoist C, Birney E, Bodenmiller B, Campbell P, Carninci P, Clatworthy M, et al. (2017). *The Human Cell Atlas*. *Elife* 6.
- Reynaert H, Urbain D, and Geerts A (2008). Regulation of sinusoidal perfusion in portal hypertension. *Anat Rec (Hoboken)* 291, 693–698. [PubMed: 18484616]
- Robinson MW, Harmon C, and O'Farrelly C (2016). Liver immunology and its role in inflammation and homeostasis. *Cell Mol Immunol* 13, 267–276. [PubMed: 27063467]
- Romero-Gomez M, Zelber-Sagi S, and Trenell M (2017). Treatment of NAFLD with diet, physical activity and exercise. *J Hepatol* 67, 829–846. [PubMed: 28545937]
- Samuel VT, and Shulman GI (2018). Nonalcoholic Fatty Liver Disease as a Nexus of Metabolic and Hepatic Diseases. *Cell Metab* 27, 22–41. [PubMed: 28867301]
- Schafer S, Viswanathan S, Widjaja AA, Lim WW, Moreno-Moral A, DeLaughter DM, Ng B, Patone G, Chow K, Khin E, et al. (2017). IL-11 is a crucial determinant of cardiovascular fibrosis. *Nature* 552, 110–115. [PubMed: 29160304]
- Sims NA, and Walsh NC (2010). GP130 cytokines and bone remodelling in health and disease. *BMB Rep* 43, 513–523. [PubMed: 20797312]
- Staels B, Rubenstrunk A, Noel B, Rigou G, Delataille P, Millatt LJ, Baron M, Lucas A, Tailleux A, Hum DW, et al. (2013). Hepatoprotective effects of the dual peroxisome proliferator-activated receptor alpha/delta agonist, GFT505, in rodent models of nonalcoholic fatty liver disease/nonalcoholic steatohepatitis. *Hepatology* 58, 1941–1952. [PubMed: 23703580]
- Tabibian JH, Masyuk AI, Masyuk TV, O'Hara SP, and LaRusso NF (2013). Physiology of cholangiocytes. *Compr Physiol* 3, 541–565. [PubMed: 23720296]
- Tabula Muris C, Overall, c., Logistical, c., Organ, c., processing, Library, p., sequencing, Computational data, a., Cell type, a., Writing, g., et al. (2018). Single-cell transcriptomics of 20 mouse organs creates a Tabula Muris. *Nature* 562, 367–372. [PubMed: 30283141]
- Tanay A, and Regev A (2017). Scaling single-cell genomics from phenomenology to mechanism. *Nature* 541, 331–338. [PubMed: 28102262]
- Trim N, Morgan S, Evans M, Issa R, Fine D, Afford S, Wilkins B, and Iredale J (2000). Hepatic stellate cells express the low affinity nerve growth factor receptor p75 and undergo apoptosis in response to nerve growth factor stimulation. *Am J Pathol* 156, 1235–1243. [PubMed: 10751349]



- van der Lienden MJC, Gaspar P, Boot R, Aerts J, and van Eijk M (2018). Glycoprotein Non-Metastatic Protein B: An Emerging Biomarker for Lysosomal Dysfunction in Macrophages. *Int J Mol Sci* 20.
- Vega-Badillo J, Gutierrez-Vidal R, Hernandez-Perez HA, Villamil-Ramirez H, Leon-Mimila P, Sanchez-Munoz F, Moran-Ramos S, Larrieta-Carrasco E, Fernandez-Silva I, Mendez-Sanchez N, et al. (2016). Hepatic miR-33a/miR-144 and their target gene ABCA1 are associated with steatohepatitis in morbidly obese subjects. *Liver Int* 36, 1383–1391. [PubMed: 26945479]
- Wang GX, Zhao XY, Meng ZX, Kern M, Dietrich A, Chen Z, Cozacov Z, Zhou D, Okunade AL, Su X, et al. (2014). The brown fat-enriched secreted factor Nrg4 preserves metabolic homeostasis through attenuation of hepatic lipogenesis. *Nat Med* 20, 1436–1443. [PubMed: 25401691]
- Wang Q, Sharma VP, Shen H, Xiao Y, Zhu Q, Xiong X, Guo L, Jiang L, Ohta K, Li S, et al. (2019). The hepatokine Tsukushi gates energy expenditure via brown fat sympathetic innervation. *Nature Metabolism* 1.
- Wang Y, Cella M, Mallinson K, Ulrich JD, Young KL, Robinette ML, Gilfillan S, Krishnan GM, Sudhakar S, Zinselmeyer BH, et al. (2015). TREM2 lipid sensing sustains the microglial response in an Alzheimer's disease model. *Cell* 160, 1061–1071. [PubMed: 25728668]
- Xiong X, Wang Q, Wang S, Zhang J, Liu T, Guo L, Yu Y, and Lin JD (2019). Mapping the molecular signatures of diet-induced NASH and its regulation by the hepatokine Tsukushi. *Mol Metab* 20, 128–137. [PubMed: 30595550]
- Zhao X, Huffman KE, Fujimoto J, Canales JR, Girard L, Nie G, Heymach JV, Wistuba II, Minna JD, and Yu Y (2017). Quantitative Proteomic Analysis of Optimal Cutting Temperature (OCT) Embedded Core-Needle Biopsy of Lung Cancer. *J Am Soc Mass Spectrom* 28, 2078–2089. [PubMed: 28752479]

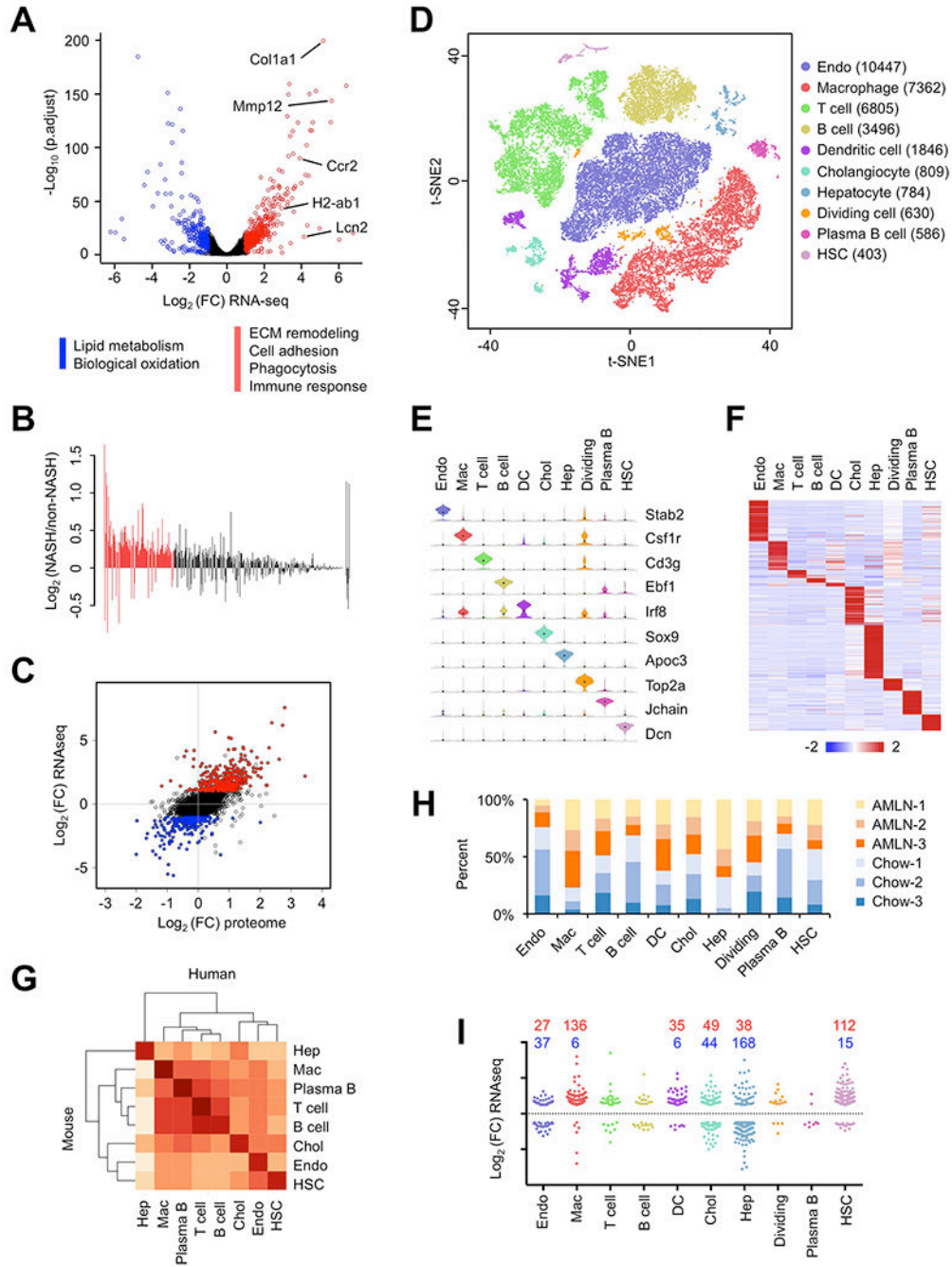


**Figure 1. Single-cell RNA-seq analysis of NPC isolated from healthy and NASH mouse livers.** (A) Volcano plot of hepatic gene expression in chow and AMLN diet-fed mice analyzed by RNA-seq of total liver mRNA. Genes upregulated or downregulated by more than 2-fold are shown in red and blue, respectively. (B) Bar graph of relative expression comparing NASH (NAS > 5.0) and non-NASH (NAS < 3.0) human livers for the list of genes upregulated in mouse NASH. Red bars denote genes differentially regulated in human NASH ( $\text{FDR} < 0.1$ ).

(C) Correlation between RNA-seq and quantitative proteomic analyses. Shown is scatter plot of log-transformed fold change (FC) of mRNA (y-axis) and protein (x-axis) expression values comparing AMLN and chow livers. Genes upregulated or downregulated by more than 2-fold in RNA-seq are indicated in red and blue, respectively.

(D) t-SNE visualization of liver cell clusters based on 33,168 single cell transcriptomes. Cell counts for endothelial cells (Endo), macrophages, T cells, B cells, DC, cholangiocytes (Chol), hepatocytes (Hep), dividing cells, plasma B cells and HSC are indicated in parentheses.

(E) Violin plots showing representative marker gene expression for each cluster.

(F) Heat map of cluster marker genes.

(G) Correlation matrix between mouse and human liver cells. Normalized average UMI values for each cell type were used in the calculation of correlation coefficient values.

(H) Percent contribution of chow (blue) and AMLN (orange) mouse liver cells from in each cluster.

(I) Cell type distribution for upregulated (red) and downregulated (blue) genes in NASH mouse (A). Each gene was assigned a cluster based on the cell type with highest expression for that gene.

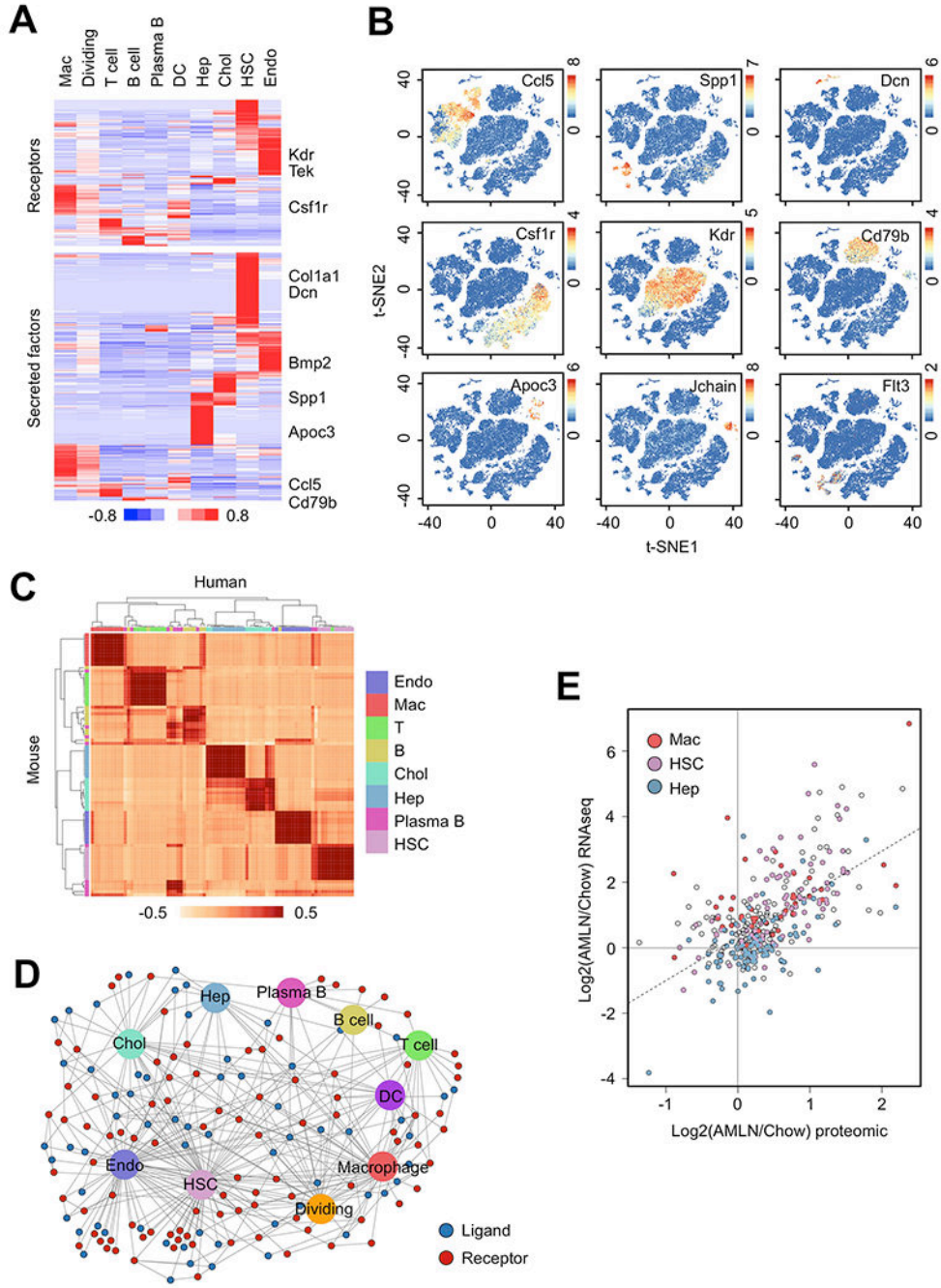


**Figure 2. Liver cell secretome gene analysis.**

(A) Heat map representation of genes expression for membrane receptors (top) and secreted factors (bottom) among liver cell types. Genes with normalized UMI values > 1.0 in at least one cluster were included in the analyses.

(B) Visualization of cell-type specific ligand and receptor gene expression.

(C) Correlation of ligand and receptor gene expression between mouse and human liver cells.

**(D)** Network visualization of ligand-receptor connectivity among different mouse liver cell types.

**(E)** Scatter plot of ligand and receptor gene expression based on RNA-seq and quantitative proteomic data. The genes with highest expression in HSC, macrophages and hepatocytes are indicated.

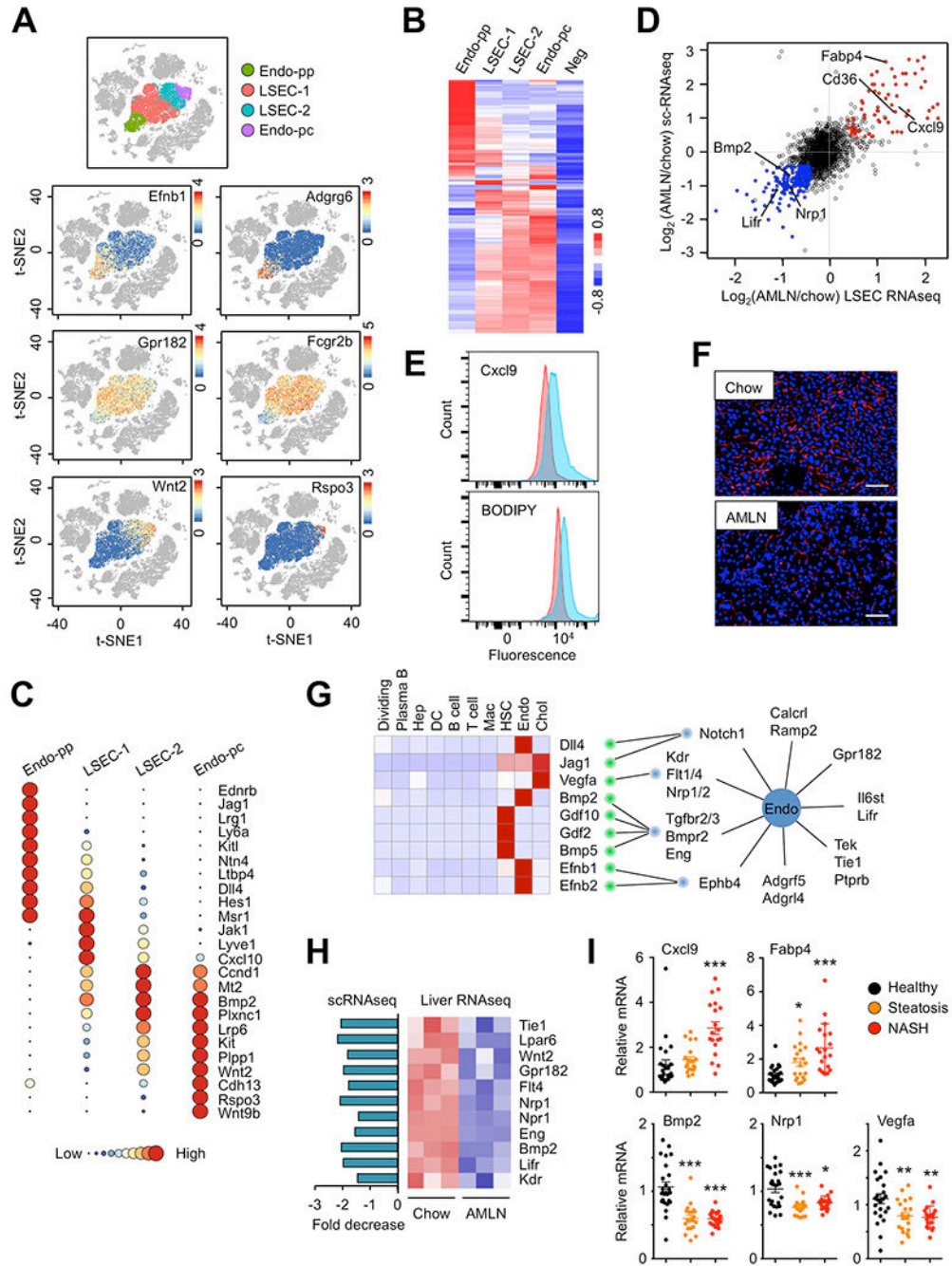


**Figure 3. Disruption of the hepatic vascular signaling network in NASH.**  
 (A) t-SNE visualization and marker gene expression in four liver endothelial subtypes.  
 (B) Clustering analysis and heat map of gene expression in four endothelial subtypes. Averaged expression values from non-endothelial clusters were used as negative background (Neg).  
 (C) Circle plots illustrating subtype-specific gene expression. Normalized average UMI values for each subcluster were represented by dot size and color intensity.



**(D)** Scatter plot of endothelial gene expression revealed by scRNA-seq of liver NPC (y-axis) and RNA-seq analysis of LSEC (x-axis) isolated from chow and AMLN mouse livers.

**(E)** Flow cytometry analysis of Cxcl9 and lipid accumulation (BODIPY) in gated LSEC from chow (red) and AMLN (blue) mouse livers.

**(F)** Anti-FCGR2B immunofluorescence staining of frozen liver sections from chow and AMLN mice (scale bar=100µm).

**(G)** The liver vascular signaling network. Shown are heat map of ligands (left) and expression of membrane receptors in the endothelial cluster (right). Red lines indicate predicted ligand-receptor pairs.

**(H)** Disruption of endothelial cell signaling network in NASH. Expression of angiocrine ligands and receptors in chow and AMLN mouse livers was analyzed by scRNA-seq (left) and liver RNA-seq (right).

**(I)** Dot plot of microarray expression values in a cohort of healthy individuals and patients with steatosis or NASH. Data were analyzed using one-way ANOVA. \*p<0.05, \*\* p<0.01, \*\*\* p<0.001 vs. healthy.

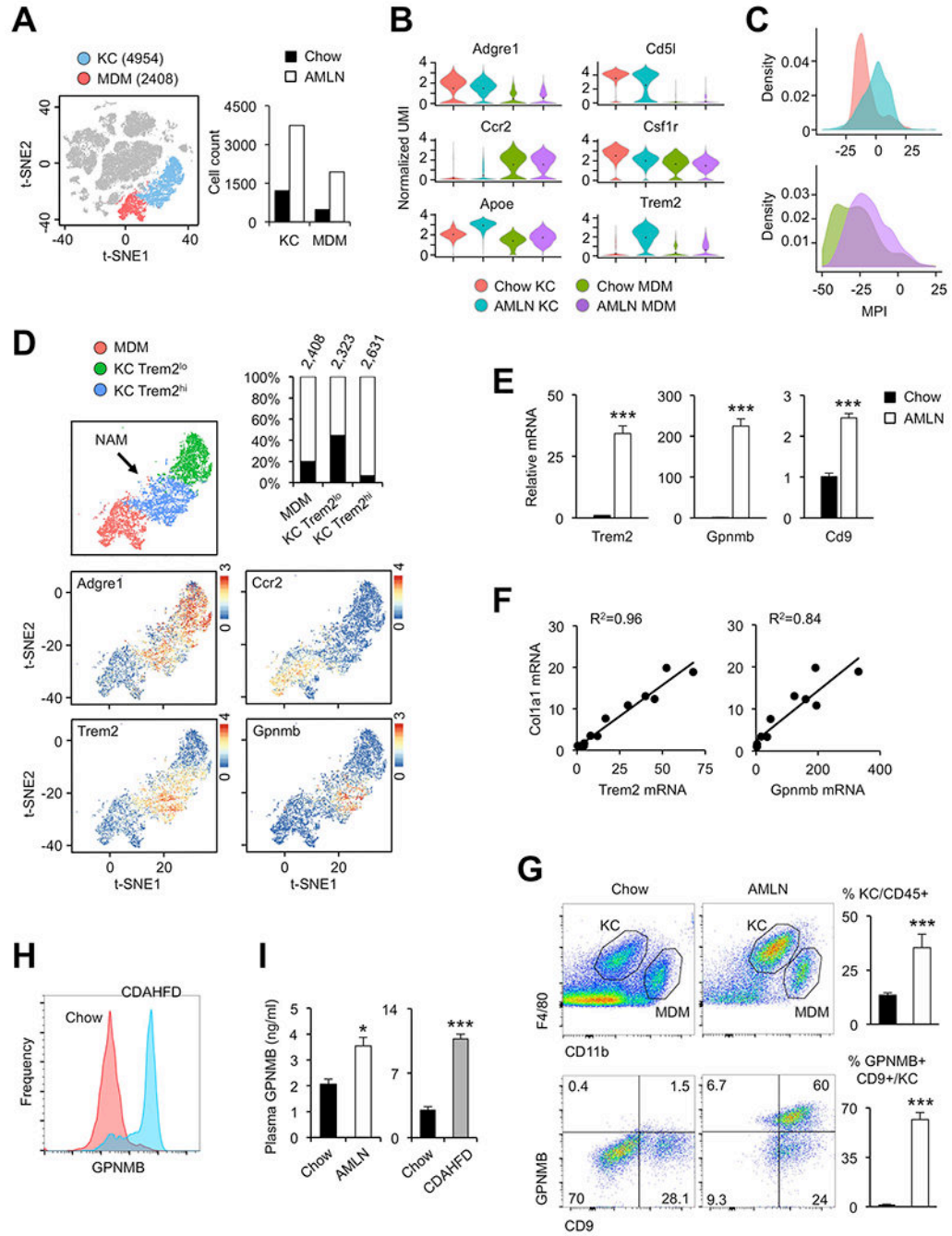


**Figure 4. Emergence of NASH-associated macrophages in the liver.**

(A) Illustration of tissue-resident Kupffer cells (KC, blue) and monocyte-derived macrophages (MDM, red). Total cell counts from chow and AMLN mouse livers for each subcluster are shown on the right (n=3).

(B) Violin plot of normalized UMI showing distribution of marker gene expression.

(C) Histogram of macrophage polarization index of liver macrophages. Cell types and diets are colored as in (B).

**(D)** t-SNE plot illustrating subpopulations of KC marked by low (green) and high (blue) Trem2 mRNA expression. Percentage contributions of chow (filled) and AMLN (open) macrophages to each subpopulation and total cell counts are indicated. Feature plots of marker gene expression are shown at the bottom.

**(E)** Whole liver qPCR analysis for NAM marker genes in mice fed chow or AMLN diet for 6 months (n=4).

**(F)** Correlation of liver gene expression in a cohort of mice fed AMLN diet for three months.

**(G)** Flow cytometry analysis of liver cells. Percentage of KC in CD45+ cells (top) and GPNMB+ CD9+ KC in mice fed chow or AMLN diet are shown (n=3).

**(H)** Histogram of GPNMB flow cytometry analysis of KC subpopulation in mice fed chow (red) or CDAHFD (blue) for 4 weeks (n=3).

**(I)** Plasma GPNMB levels measured by ELISA comparing chow with AMLN mice (n=10) or chow with CDAHFD mice (n=5). Data in (E), (G), and (I) represent mean  $\pm$  SEM.

\*p<0.05, \*\*p<0.01, \*\*\*p<0.001 vs. chow; two-tailed unpaired Student's t-test.

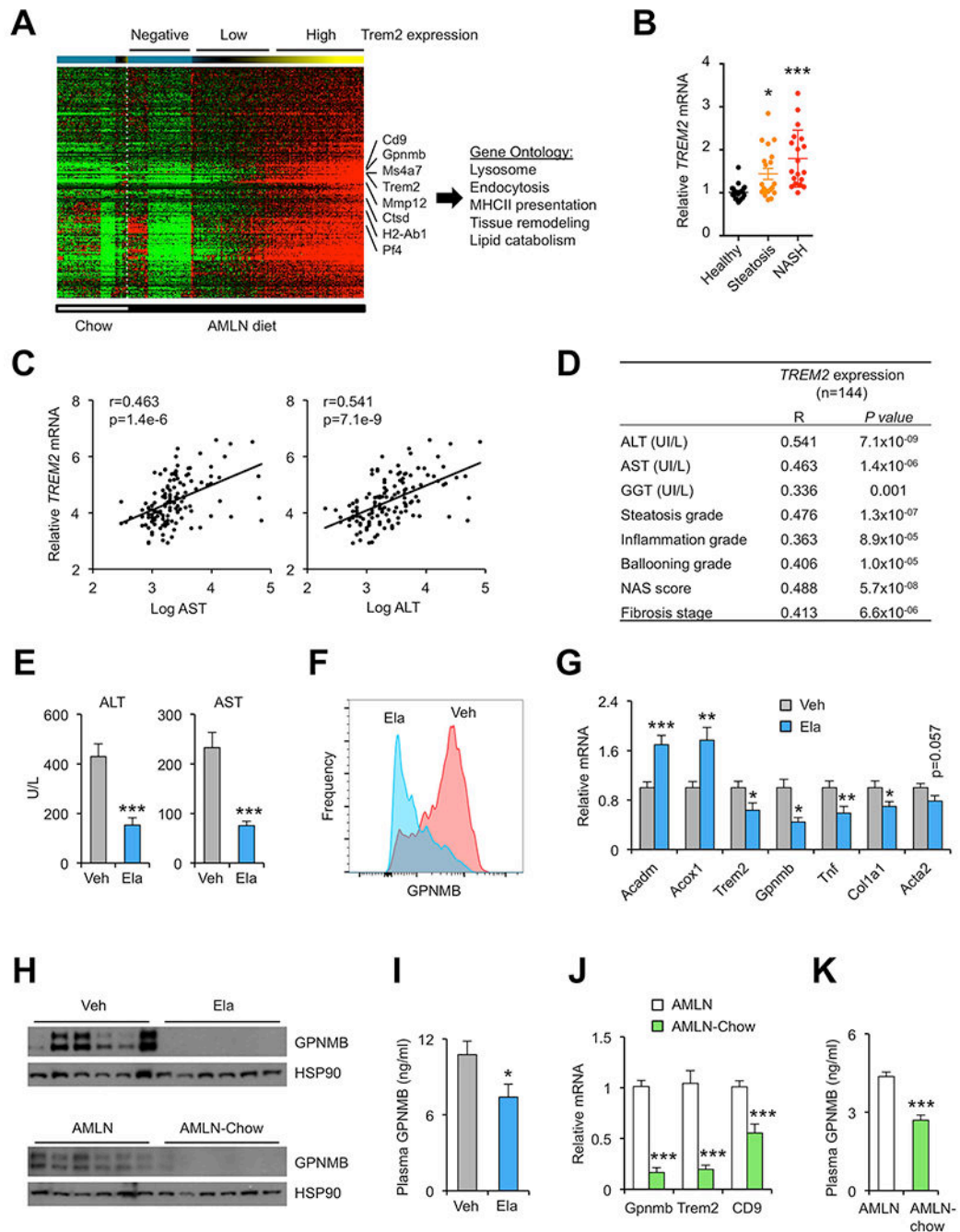


**Figure 5. Dynamic regulation of NAM in human NASH and during NASH resolution.**

(A) Heat map representation of macrophage gene expression. Cells were ordered by increasing Trem2 expression and binned per 25 cells for analysis. A cluster of genes positively correlated with Trem2 is shown.

(B) Dot plot of microarray expression values for Trem2 in a cohort of healthy individuals and patients with steatosis or NASH. Data represent mean  $\pm$  SE and were analyzed using one-way ANOVA. \* $p < 0.05$ , \*\*  $p < 0.01$ , \*\*\*  $p < 0.001$ .

- (C) Association between liver *TREM2* mRNA expression and plasma AST and ALT levels in a cohort of 144 NASH patients.
- (D) Association between liver *TREM2* mRNA expression and NASH parameters in the human patient cohort.
- (E) Plasma ALT and AST concentrations in CDAHFD-fed mice gavaged daily with vehicle (Veh) or Elafibranor (Ela) for 24 days (n=10).
- (F) Flow cytometry analysis of GPNMB expression in KC isolated from treated mice (n=3).
- (G) qPCR analysis of liver gene expression.
- (H) Immunoblots of whole liver extracts in mice from (E) (top) and extracts from mice fed AMLN diet for six months (AMLN) or four months followed by chow for two months (AMLN-chow) (bottom).
- (I) Plasma GPNMB levels.
- (J) qPCR analysis of liver gene expression in mice fed AMLN diet for six months (AMLN) or four months followed by chow for two months (NASH-chow).
- (K) Plasma GPNMB levels in mice from J. Data in (E), (G) and (I-K) represent mean  $\pm$  SEM. \*p<0.05, \*\*p<0.01, \*\*\*p<0.001 vs. chow; two-tailed unpaired Student's t-test.

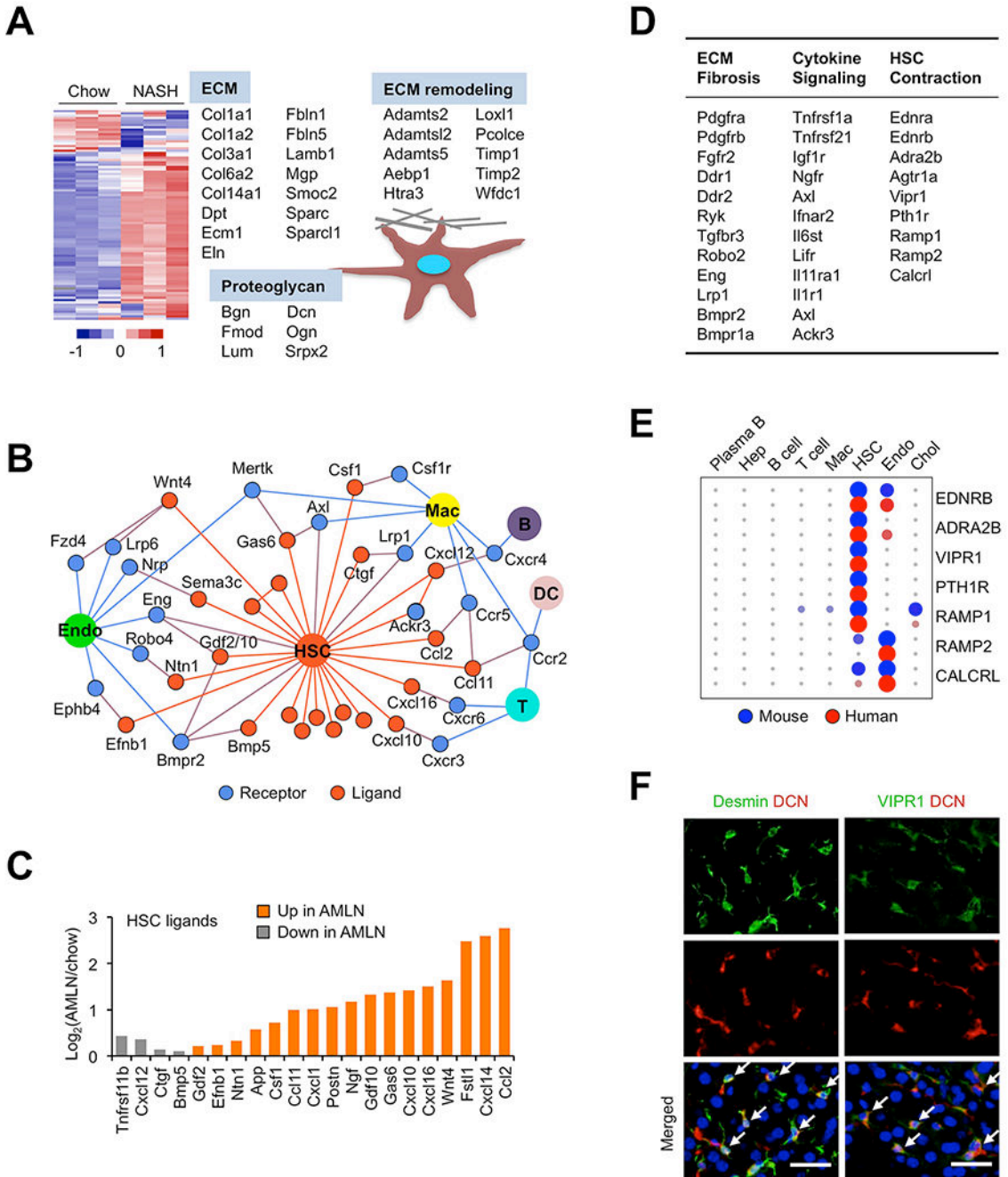


**Figure 6. Landscape of the HSC signaling network.**

(A) Heat map representation of HSC-enriched secretome genes using liver RNA-seq data from chow and AMLN mice. Genes encoding structural proteins of ECM and those involved in ECM remodeling are indicated.

(B) The HSC secretome. Ligands exhibiting > 3-fold enriched expression in the HSC cluster are shown in orange with their known receptors indicated in blue. The ligand-receptor pairs are shown when receptor expression was observed in at least one cluster (normalized UMI>1.0) based on the scRNA-seq dataset.



(C) Regulation of stellakine gene expression in NASH. Average expression values from chow and AMLN liver RNA-seq dataset were used.

(D) The HSC-enriched membrane receptors.

(E) Circle plot of receptor gene expression in mouse and human liver cells.

(F) Immunofluorescence staining of frozen liver sections using antibodies indicated at the top. Nuclei were stained using DAPI (blue). Arrows indicate co-localization of protein expression in HSC (scale bar=50 $\mu$ m).

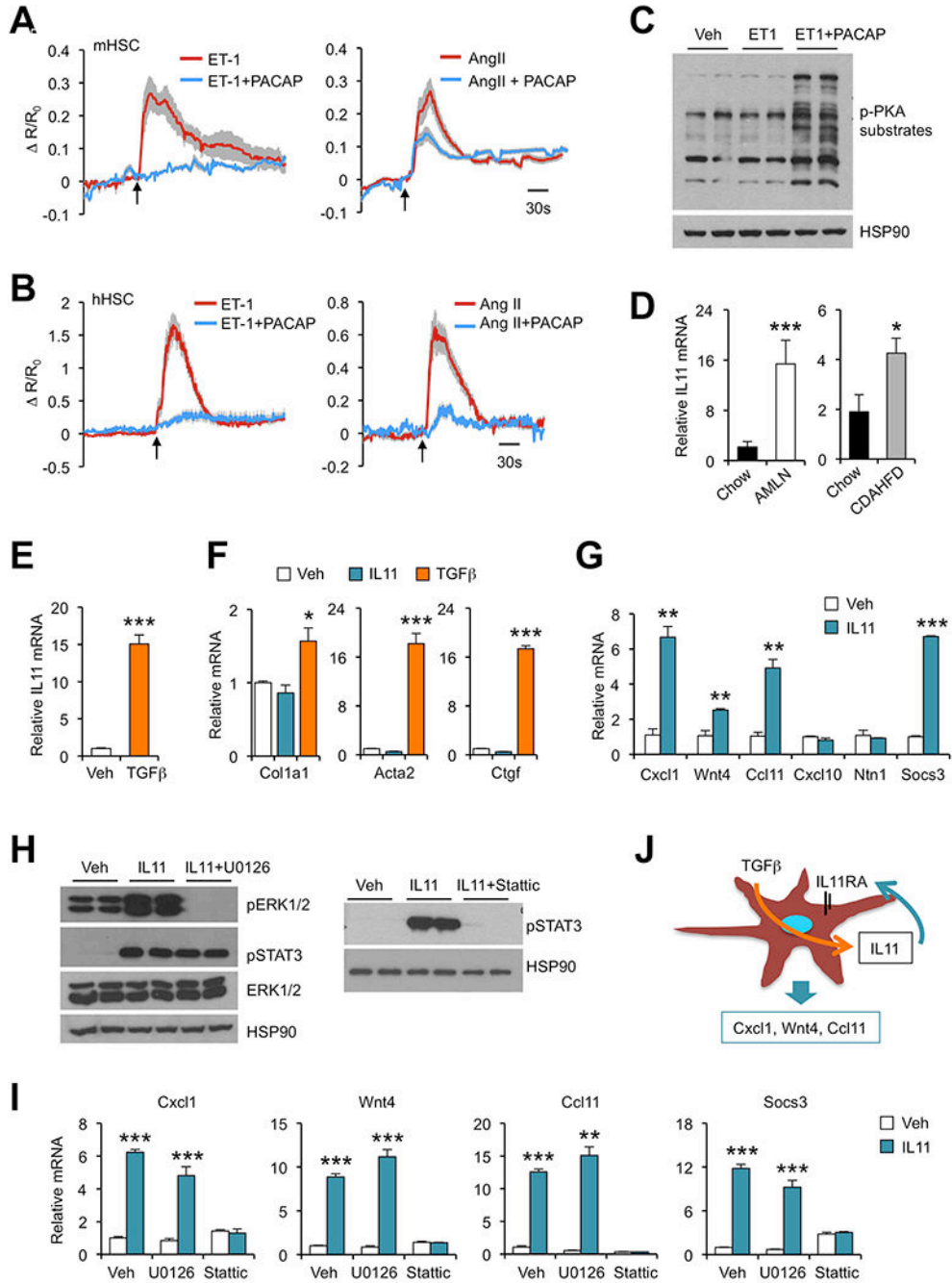


**Figure 7. Functional analysis of vasoactive hormone signaling and the autocrine IL11 loop in HSC.**

(A) Averaged intracellular calcium traces of primary mouse HSC treated with 100 nM of ET-1 (n=14), ET-1 plus 100 nM of PACAP (n=30), 100 nM of Ang II (n=25) or Ang II plus PACAP (n=41).

(B) Averaged intracellular calcium traces of primary human HSC treated with 100 nM ET-1 (n=23), ET-1 plus 100 nM of PACAP (n=16), 100 nM of Ang II (n=21) or Ang II plus PACAP (n=21). Arrows indicate initiation of treatments. Data represent mean  $\pm$  SD.

- (C) Immunoblots of mouse HSC lysates treated with vehicle (Veh), ET-1 or ET-1 plus PACAP for 10 min.
- (D) qPCR analysis of liver Il11 expression in mice fed chow (n=4) or AMLN diet (n=4) for six months. A separate cohort of mice was fed chow (n=5) or CDAHFD (n=5) for four weeks.
- (E) qPCR analysis of Il11 expression in immortalized mouse HSC treated with Veh or TGF $\beta$  (5 ng/ml) for 24 hrs.
- (F) qPCR analysis of gene expression in immortalized mouse HSC treated with Veh, IL11 (100 ng/ml) or TGF $\beta$  (5 ng/ml) for 24 hrs.
- (G) qPCR analysis of gene expression in immortalized mouse HSC treated with Veh or IL11 (100 ng/ml) for 4 hrs.
- (H) Immunoblots of total lysates from immortalized mouse HSC treated for 10 min.
- (I) qPCR analysis of gene expression in immortalized mouse HSC treated with Veh or IL11 without or with U0126 (20 nM) or Stattic (20  $\mu$ M).
- (J) Regulation of stellakine gene expression by autocrine IL11 signaling in HSC.

## KEY RESOURCES TABLE

REAGENT or RESOURCE	SOURCE	IDENTIFIER
<b>Chemicals, Peptides, and Recombinant Proteins</b>		
Pronase	Sigma	P5147
Collagenase type II	Worthington	LS004196
DNase I	Roche	R104159001
Optiprep	Axis Shield	1114542
CD11b magnetic beads	Miltenyi Biotech	130-093-634
CD146 magnetic beads	Miltenyi Biotech	130-092-007
Recombinant Mouse IL-11 Protein	R&D Systems	418-ML
Recombinant, Mouse TGF beta 1	Thermo Fisher	50-112-2731
Endothelin 1	R&D Biosystems	1160
Angiotensin II	R&D Biosystems	1158
PACAP 38	Phoenix Pharmaceuticals	052-05
Elafibranor	Axon Medchem	Axon 2727
Stattic	Cayman Chemical	14590
Mek inhibitor U0126	LC Laboratories	U-6770
<b>Antibodies</b>		
Rabbit Polyclonal anti-Desmin	Thermo Fisher	RB-9014-P
Goat polyclonal anti-Decorin	R&D Biosystems	AF1060
Alexa Fluor 488-conjugated donkey polyclonal anti-rabbit IgG	Jackson Immuno Research	711545152
Rhodamine Red-X-conjugated donkey polyclonal anti-goat IgG	Jackson Immuno Research	705295147
Goat polyclonal anti-FCGR2B	gifts from Dr. Glenn Dorsam	N/A
Rabbit polyclonal anti-VIPR1 <sup>47</sup>	gifts from Dr. Mark Coggeshall	N/A
Rabbit polyclonal anti-phospho-Stat3 (Tyr705)	Cell Signaling Technology	9131
Rabbit polyclonal anti-phospho-p44/42 MAPK(Erk1/2) (Thr202/Tyr204)	Cell Signaling Technology	4370
Rabbit Monoclonal anti-p44/42 MAPK(Erk1/2) (137F5)	Cell Signaling Technology	4695
Rabbit Monoclonal anti-phospho-PKA substrate (RRXS/T)(100G7E)	Cell Signaling Technology	9624
Rabbit polyclonal anti-HSP90 $\alpha/\beta$	Santa Cruz BioTech	sc-7947
Goat polyclonal anti-Osteoactivin/GPNMB	R&D Biosystems	AF2330
PerCP anti-mouse CD45 Antibody Clone 30-F11	Biologend	103130
APC anti-mouse CD146 Antibody Clone ME-9F1	Biologend	134711
PE anti-mouse CD36 Antibody Clone HM36	Biologend	102605
PE anti-mouse CXCL9 (MIG) Antibody Clone MIG-2F5.5	Biologend	515603

REAGENT or RESOURCE	SOURCE	IDENTIFIER
Alexa Fluor® 700 anti-mouse CD45 Antibody Clone I3/2.3	Biolegend	147716
PE/Cy7 anti-mouse F4/80 Antibody Cone BM8	Biolegend	123114
APC/Cy7 anti-mouse/human CD11b Antibody Clone M1/70	Biolegend	101226
PE anti-mouse CD9 Antibody Clone MZ3	Biolegend	124805
GPNMB Monoclonal Antibody (Clone CTSREVL)	Thermo Fisher Scientific Asheville LLC	50-5708-82
Rat IgG2a kappa Isotype Control (Clone eBR2a)	Thermo Fisher Scientific Asheville LLC	50-4321-82
<b>Oligonucleotides</b>		
Gene		
NASH KC and hepatokine primers	This paper Table S7	N/A
<b>Critical Commercial Assays</b>		
Stanbio ALT/SGPT Liqui-UV Test	Stanbio	2930
Stanbio AST/SGOT Liqui-UV Test,	Stanbio	2920
Mouse Osteoactivin/GPNMB DuoSet ELISA	R&D Biosystems	DY2330
<b>Experimental Models: Cell Lines</b>		
Human HSC	Sciencell	5300
Mouse immortalized HSC	This paper	N/A
<b>Experimental Models: Organisms/Strains</b>		
C57BL/6J	Jackson Laboratory	JAX: 000664
<b>Deposited Data</b>		
mouse liver single cell RNA-seq (raw data and processed data)	This paper	GSE129516
mouse total liver RNA-seq (raw data and processed data)	This paper	GSE119340
mouse LSEC RNA-seq (raw data and processed data)	This paper	GSE119340
human liver microarray	NCBI Gene Expression Omnibus	GSE89632
human liver single cell RNA seq	NCBI Gene Expression Omnibus	GSE115469
Raw Blot images	This paper	<a href="https://data.mendeley.com/datasets/4dmtjj97m8/draft?a=3a5e3b11-8aba-4d22-81ff-23385848aa96http://dx.doi.org/10.17632/4dmtjj97m8.1">https://data.mendeley.com/datasets/4dmtjj97m8/draft?a=3a5e3b11-8aba-4d22-81ff-23385848aa96http://dx.doi.org/10.17632/4dmtjj97m8.1</a>
<b>Software and Algorithms</b>		
Cell Ranger	10x Genomics	<a href="https://www.10xgenomics.com/">https://www.10xgenomics.com/</a>
STAR	PMID 23104886	<a href="https://github.com/alexdobin/STAR">https://github.com/alexdobin/STAR</a>
HTSeq	PMID 25260700	<a href="https://htseq.readthedocs.io/en/release_0.11.1/#">https://htseq.readthedocs.io/en/release_0.11.1/#</a>
DESeq2	PMID 25516281	<a href="https://bioconductor.org/packages/release/bioc/html/DESeq2.html">https://bioconductor.org/packages/release/bioc/html/DESeq2.html</a>
Seurat	PMID 29608179	<a href="https://satijalab.org/seurat/">https://satijalab.org/seurat/</a>
R	The R Foundation	<a href="https://www.r-project.org/">https://www.r-project.org/</a>
Java TreeView		<a href="http://jtreeview.sourceforge.net/">http://jtreeview.sourceforge.net/</a>